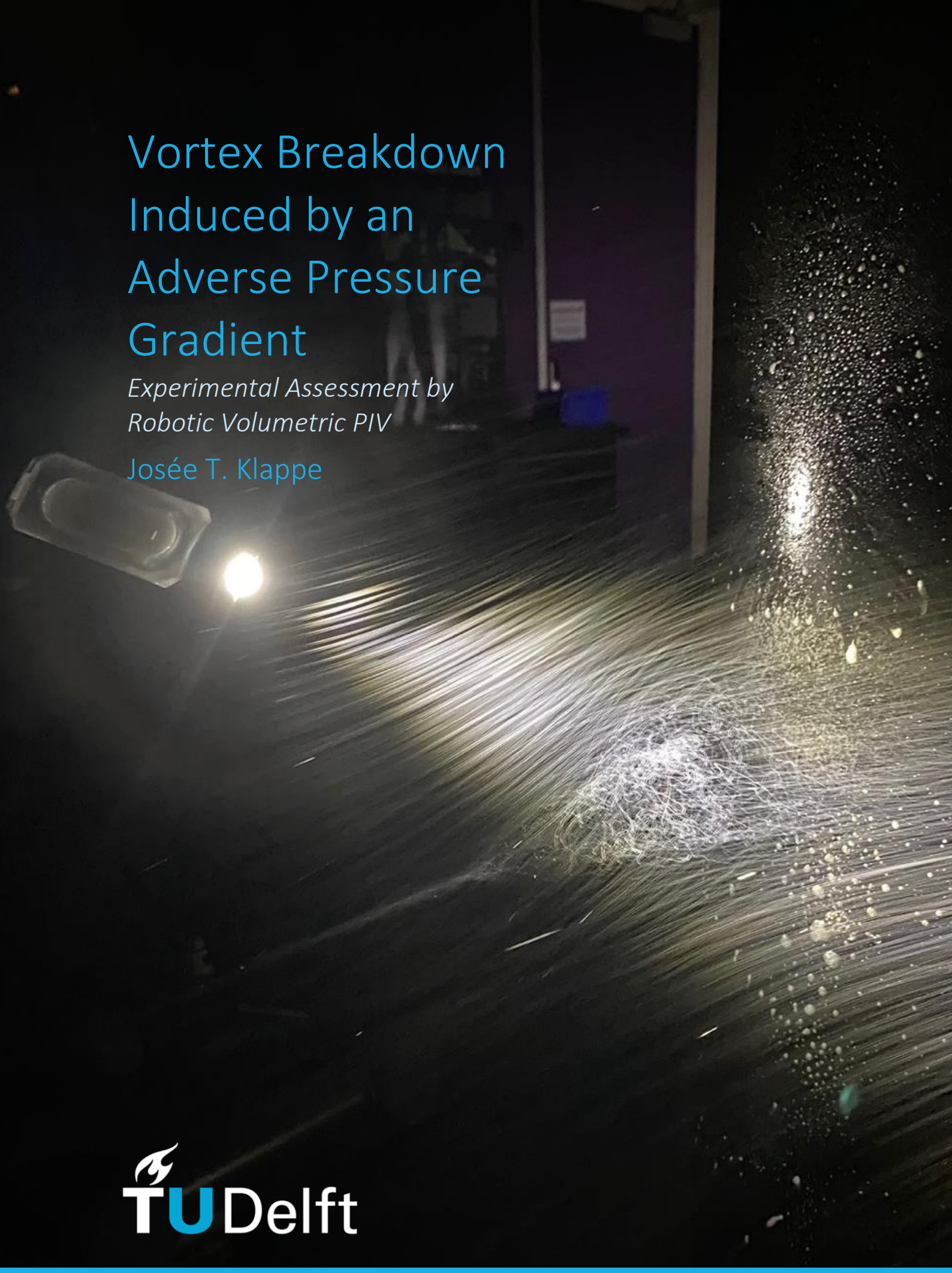

Vortex Breakdown Induced by an Adverse Pressure Gradient

Experimental Assessment by Robotic Volumetric PIV

Josée T. Klappe

TU Delft

Faculty of Aerospace Engineering

Vortex Breakdown Induced by an Adverse Pressure Gradient

Experimental Assessment by Robotic Volumetric PIV

by

Josée T. Klappe

to obtain the degree of Master of Science
at the Delft University of Technology,
to be defended publicly on Wednesday April 26th, 2023 at 13:30.

Student number:	4571940	
Project Duration:	June 10th, 2022 – April 26th, 2023	
Thesis Committee:	Prof. Dr. F. Scarano	TU Delft, chair of assessment committee
	Dr. A. Sciaccitano	TU Delft, daily supervisor
	Dr. W. Yu	TU Delft, committee member
	A. Grille Guerra, MSc	TU Delft, supervisor

An electronic version of this thesis is available at http://repository.tudelft.nl/.

Preface

As a little sister of someone who is very, very close to obtaining her Ph.D. doctorate, I have learned by a healthy-dose of comparing, that I might not be fit for a career in academia. I would like to recall a conversation I had with her at the beginning of my thesis project.

'… Eva, I think research is difficult.'

'Well, if you can design parts for an F1 car, you can do this. It's the same, think about what you want, make the design – or do the research in this case, and revisit your design until you are sure it works in every case and compare it to existing literature before finishing it.'

'But that's not how my brain works... I think if I had to design the concept of a chair and it would stand with three legs – we would never have four-legged chairs.'

Well, approximately 30 weeks later, here we are. My first four-legged chair.

I would like to thank everyone that helped me during my thesis work: my supervisors, *Andrea Sciacchitano, Fulvio Scarano,* and *Adrian Grille Guerra,* the lab technicians, *Dennis Bruikman, Peter Duyndam,* and *Frits Donker Duyvis,* the helpful *Colette Russo*, and of course my friends and family – and most importantly my sister, because this thesis is *mede mogelijk gemaakt door Eva.*

Many thanks to everyone (and everyone I forgot to mention),

Groetjes,

Josée T. Klappe,
April 2023

Abstract

Understanding and predicting vortex behavior is crucial to maximize performance using aerodynamic design. Vortex breakdown can be induced to benefit the flow field or has to be prevented to avoid losing performance. It is therefore important to study the dynamics of vortex breakdown.

The main objective of this thesis was to assess the feasibility of measuring a free, streamwise vortex and its breakdown from data acquired with robotic volumetric Particle Image Velocimetry (PIV), whilst analyzing the relation between the local flow properties and the location of the breakdown. Experiments were conducted at the W-Tunnel at the TU Delft High-Speed Lab, where vortex breakdown was induced by the adverse pressure gradient field in front of a cylinder. The robotic Coaxial Volumetric Velocimeter (CVV) was used to assess the feasibility of using this system for vortex breakdown identification, in combination with data processing using a Lagrangian Particle Tracking (LPT) technique (Shake-The-Box), to detect and analyze vortices and their breakdown. The results of this experimental campaign were analyzed to identify vortices and their breakdown from the CVV data by characterizing the vortex's internal structure. The analysis included establishing the relations of the adverse pressure gradient and the Reynolds number with the breakdown location.

The results showed that vortex breakdown is induced by the adverse pressure gradient. However, the breakdown location is not solely dependent on it. Furthermore, the effect of the Reynolds number at the breakdown location is barely measurable with the robotic volumetric PIV system.

This exploratory and experimental study showed that the CVV in combination with LPT can be used to recognize the structure of the vortex in both its pre- and post-breakdown regimes. However, for the analysis of vortex breakdown, it was found that the data was affected by the low spatial resolution. Thus, robotic volumetric PIV cannot provide conclusive results in terms of the relation between the location breakdown and local flow properties. Several recommendations regarding the experimental set-up are given for future research.

Content

Nomenclature

Latin Symbols

A, S	Area	[m^2]
C	Coefficient	[-]
D, d	Diameter	[m]
$\boldsymbol{n}$	Unit vector	[-]
p	Static pressure	[Pa]
q	Dynamic pressure	[Pa]
r	Radius	[m]
$\bar{r}$	Normalized radius, $= r/r_c$	[-]
Re	Reynolds number	[-]
$\boldsymbol{S}$	Strain rate tensor	[1/s]
t	Time	[s]
U	Velocity (freestream)	[m/s]
u, v, w	Velocity components in x, y, and z	[m/s]
x	Length	[m]
x, y, z	Cartesian axes	

Greek Symbols

α	Angle of attack	[∘]
β	Tomographic aperture	[∘]
Γ	Circulation, vortex strength	[m^2/s]
Δ	Delta, difference	[-]
θ	Angle	[∘]
ν	Kinematic viscosity	[m^2/s]
ρ	Density	[kg/m^3]
ϕ	Velocity potential	[-]
$\boldsymbol{\Omega}$	Vorticity tensor	[1/s]
Ω	Normalized circulation	[-]
$\boldsymbol{\omega}$	Vorticity	[1/s]
∇	Gradient	[-]

Superscripts

$*$	Normalized

Subscripts

θ	Tangential
∞	Freestream
axial	Axial
bd	Breakdown
c	(Vortex) core
cyl	Cylinder
max	Maximum value
p	Pressure
r	Radial
x, y, z	Cartesian axes

Abbreviations

CVV	Coaxial Volumetric Velocimeter
FSU	Fluid Supply Unit
HFSB	Helium Filled Soap Bubbles
HTA	Heavier-than-air
LPT	Lagrangian Particle Tracking
LTA	Lighter-than-air
PIV	Particle Image Velocimetry
STB	Shake-the-Box
Tomo-PIV	Tomographic Particle Image Velocimetry

List of Figures

1. Introduction

In the aerospace and motorsport industry, advanced aerodynamic design is important to maximize performance. This performance is based on maximizing lift, or downforce, whilst minimizing drag. To achieve high performance, the shape of the wings is optimized to meet the design objectives. Additionally, vortices can be used to manipulate the flow field. Vortices are often characterized as local swirling flow with a pressure minimum in its center (Jeong & Hussain, 1995). Vortices are generated when flow separates from a body, the vorticity escapes the boundary layer, and the viscous flow sheet rolls up and springs into the outer non-dissipative flow (Délery, 1994; Mitchell & Délery, 2001).

Vortices can be used to increase the performance of swept-wing aircraft. Figure **1.1** shows the difference in wing planform for an un-swept and swept-wing aircraft. For such aircraft, a vortex can be located over the wing to relieve the boundary layer of the outboard wing from the boundary layer cross-flow originating at the inboard wing, thus preventing tip stall (Obert, 2009). However, analogous to boundary layers, vortices can transition to unsteady and turbulent phenomena, also known as vortex breakdown (Mitchell & Délery, 2001). When a vortex breaks down while traveling over the wing of an aircraft, it increases in size and the increase in turbulence can negatively impact the wings' aerodynamic field (Nieuwstadt, Boersma, & Westerweel, 2016). This interaction can cause asymmetry between the performance of both wings and may induce an unwanted rolling moment (Délery, 1994; Heyes & Smith, 2005).

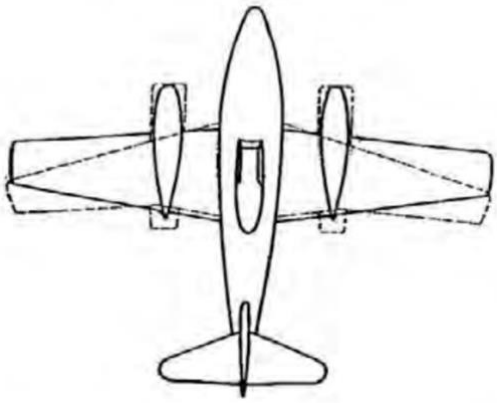

***Figure 1.1**: Messerschmitt 262 with the original, un-swept wing as solid line and its final, swept wing as dashed line. Adapted from Obert (Obert, 2009).*

Contrary, vortex breakdown can be beneficial to the flow field. If a vortex originating from a big aircraft does not break down, smaller trailing aircraft may interact with this strong vortex (Délery, 1994). Figure **1.2** illustrates that this is dangerous and could lead to rolling, loss of altitude, or structure load factors, and possibly to the crash of the smaller aircraft (Rossow, 1999). Therefore, it is desired to understand and predict these vortex dynamics when developing aerodynamic surfaces.

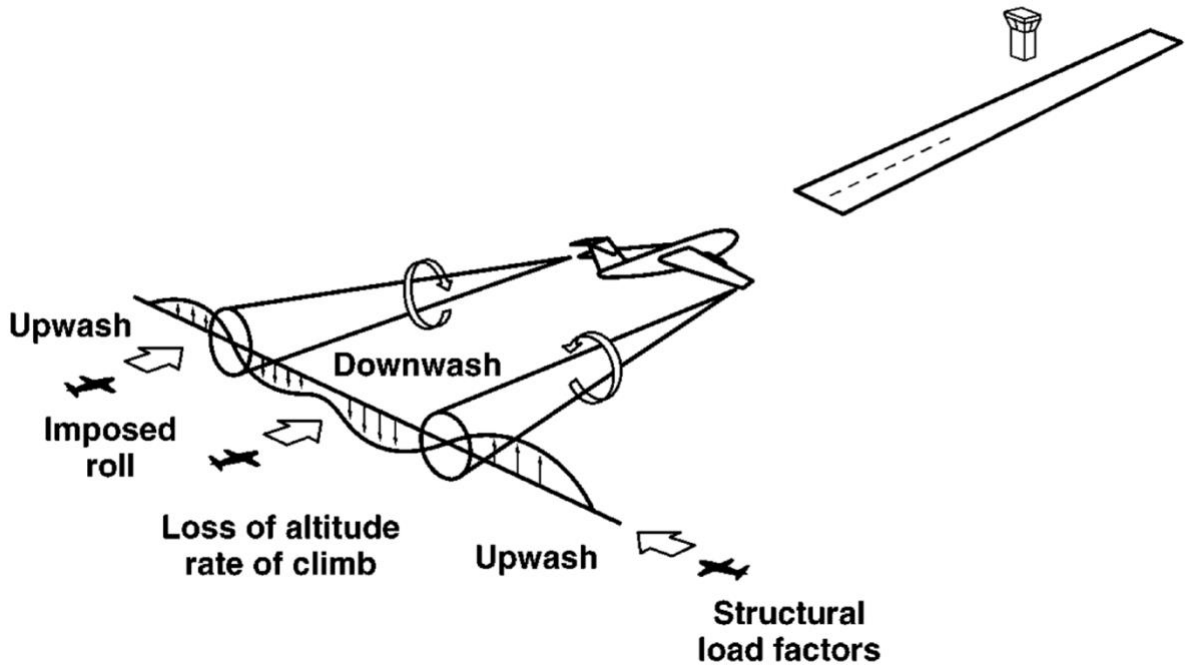

Figure 1.2: Possible encounters with the lift-generated wake for trailing aircraft (Rossow, 1999).

Previous research showed the importance of understanding vortices and vortex breakdown (Escusier, 1988; Délery, 1994). For example, Figure **1.3** shows the vortex breakdown in a water tank with an increasing adverse pressure gradient. A common observation at vortex breakdown is that the vortex structure grows rapidly in size. This means that its region of influence increases, which has a negative effect on, for example, the lift production over a wing. Most experimental studies were based on the effects of breakdown on the aerodynamic performance of wings or on the relation between flow properties and the breakdown location (Sarpkaya, On Stationary and Travelling Vortex Breakdowns, 1971; Sarpkaya, Vortex Breakdown in Swirling Conical Flows, 1971; Sarpkaya, Effect of the Adverse Pressure Gradient on Vortex Breakdown, 1974; Escusier, 1988). It was found that vortex breakdown is dependent on a number of flow properties, such as the aforementioned adverse pressure gradient and the Reynolds number (Sarpkaya, Effect of the Adverse Pressure Gradient on Vortex Breakdown, 1974; Délery, 1994).

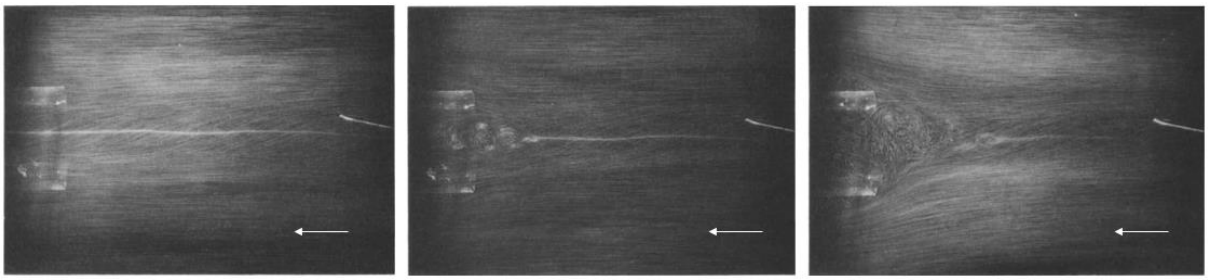

Figure 1.3: Breakdown of a free vortex in a water tunnel experiment with increasing adverse pressure gradient from left to right. The direction of the freestream is indicated with the white arrow. Adapted from Delery (Délery, 1994).

Adverse pressure gradients are a common occurrence in aerodynamic design. When looking at fundamental problems, a widely known adverse pressure gradient is the pressure recovery over the suction side of an airfoil. In applied problems, this translates to the pressure recovery over the wings of aircraft and on a number of aerodynamic elements on racecars. For complex applications, the adverse pressure gradient will interact with other elements, such as vortices emanating from upstream elements. To maximize performance, it is of utmost importance that these vortices do not break down and interfere with the pressure field of other elements. Therefore, understanding this interaction is the topic of interest.

The interaction of adverse pressure gradients and vortex breakdown has been a topic of research in the past. Experiments were conducted using confined vortices and diverging ducts in a water tank (Sarpkaya, Effect of the Adverse Pressure Gradient on Vortex Breakdown, 1974). From this experiment, it was concluded that the vortex breakdown was dependent on the adverse pressure gradient, the Reynolds number, and the circulation. However, the results for the adverse pressure gradient were affected by the boundary layer separating in the ducts. Furthermore, to aid in understanding and predicting vortex breakdown within the aerospace and motorsport industry, it is crucial to study free, streamwise vortices and their breakdown in airflow. To the best of the author's knowledge, no research has been done on free, streamwise vortices and the effect of local flow parameters on their breakdown location.

Vortex breakdown is a turbulent phenomenon and turbulence is intrinsically three-dimensional. So, to successfully conduct experiments in pursuit to understand vortex breakdown, it is of vital importance to use a flow measurement technique that can reconstruct the three-dimensional flow field. Innovations in Particle Image Velocimetry (PIV) led to the ability to reconstruct a three-dimensional flow field. PIV is enhanced to use multiple cameras and a voxel-based algorithm to obtain three-dimensional data (Elsinga, Scarano, Wieneke, & van Oudheusden, 2006). Three-dimensional PIV is computationally expensive, needs optical access, and has a large set-up. For this reason, a coaxial configuration of the illumination and cameras was developed, which is called a Coaxial Volumetric

Velocimeter (CVV) (Schneiders, Scarano, Jux, & Sciacchitano, 2018). Three-dimensional flow fields were reconstructed by using the robotic operation of the CVV, a Lagrangian Particle Tracking (LPT) algorithm (Shake-The-Box), and the use of different tracing particles with regards to PIV (Jux, Sciacchitano, Schneiders, & Scarano, 2018). The combination of both CVV and LPT is often referred to as robotic volumetric PIV. Experimental research concluded that robotic volumetric PIV compared well to the literature in terms of the reconstructed flow topology (Jux, Sciacchitano, Schneiders, & Scarano, 2018). However, no experimental study using this technique has been conducted into the physics of free vortices and vortex breakdown.

This thesis aims to assess the feasibility of measuring a free, streamwise vortex and its breakdown from data acquired with robotic volumetric PIV, whilst analyzing the relation between the local flow properties and the location of the breakdown. To be able to find conclusive results for this two-fold research objective, this experimental and explorative study will be divided into the following sub-questions:

1. How to detect and characterize a free, streamwise vortex and its breakdown from a robotic volumetric PIV experiment?
2. Can the relation between the location of the breakdown and the local flow properties (i.e., the adverse pressure gradient and the Reynolds number) be established?

A literature review will be presented on the topic of vortex dynamics in Chapter 2. Here, a description of the general concept of vortices and their breakdown is given. Research of Sarpkaya on the effect of adverse pressure gradients on vortex breakdown will be elaborated upon (1974). A review of the latest flow measurement techniques which can reconstruct a flow field in three dimensions is presented in Chapter 3. After that, the methodology of this thesis' experimental campaign is described in Chapter 4. Followed by a discussion of the results in Chapter 5. Last, conclusions and recommendations can be found in Chapter 6.

2. Vortex Dynamics

In this chapter is the general concept of vortices discussed. Vortex models, vortex identification methods, and the principle of vortex breakdown are presented. Previous research into the effects of an adverse pressure gradient on vortex breakdown will be elaborated upon.

2.1 General Concept

Vortices are often described as local swirling flow. Wingtip vortices of aircraft originate as the flow from the high-pressure area below the wing 'folds' towards the low-pressure area at the upper surface of the wing. In combination with the forward motion of the aircraft, is this folding recognized as a streamwise vortex. In other words: vortices are generated when flow separates from a body, the vorticity escapes the boundary layer, and the viscous flow sheet rolls up and springs into the outer non-dissipative flow (Délery, 1994; Mitchell & Délery, 2001). There are two main types of vortices, depending on how the separation was induced to the body: vortices in front of a blunt body, commonly known as horseshoe vortices, and vortices forming behind an obstacle, also known as tornado like vortices (Mitchell & Délery, 2001). For a visual representation of these vortices, see Figure **2.1**. As shown, from the vortical structure, the roll up from the separation surface can be recognized (Délery, 1994).

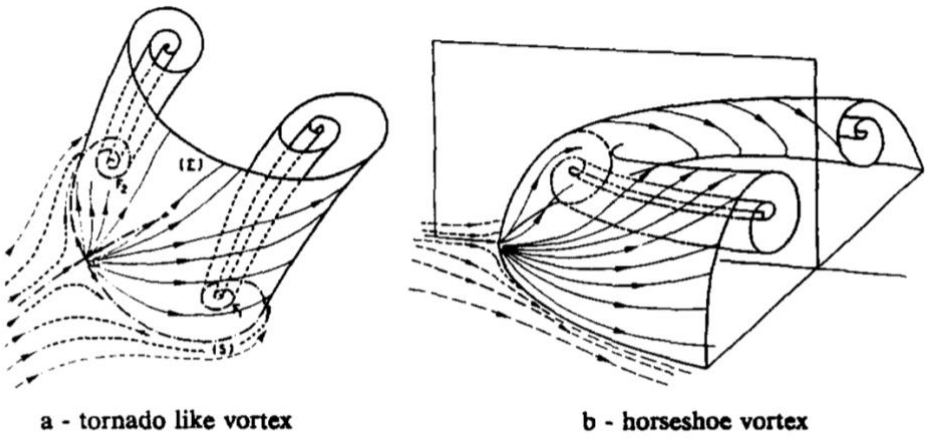

Figure 2.1: Vortical structure formation (Délery, 1994)

A vortex is characterized by its axial and tangential velocity components, U_{axial} and U_θ, respectively. The radial component, U_r, is usually considered zero. The axial velocity component can either be smaller than the freestream velocity at the core, which is a so-called wake-like vortex, or greater than the freestream velocity, which is the jet-like case (Délery, 1994).

A common vortex is the wing tip vortex of aircraft. These vortices originate from the pressure difference between the upper and lower surface of the wing, i.e. the lift production, and are thus inevitable. These can be hazardous, as smaller aircraft flying in a wake of another aircraft, could experience an unwanted rolling moment (Délery, 1994). Figure **2.2** illustrates the formation of a wing tip vortex as a cross-stream plane (Heyes & Smith, 2005). The plane in Figure **2.2** is obtained using Particle Image Velocimetry. This study was focused on modifying the wing tip vortex to reduce the rolling moment on the following aircraft.

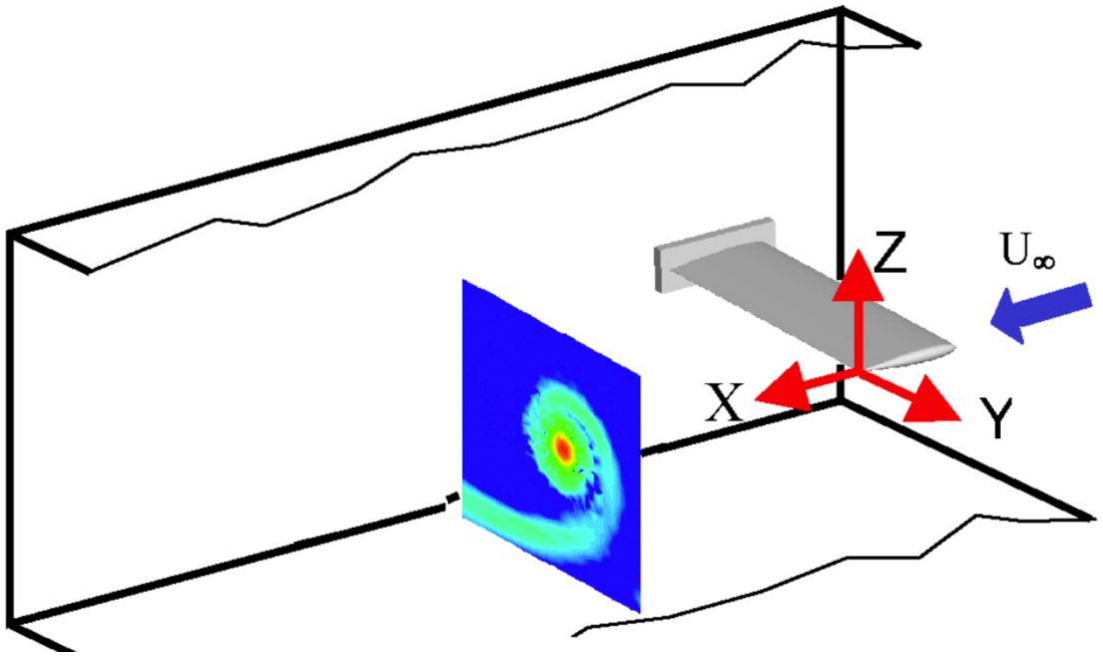

***Figure 2.2**: Experimental set-up including a cross-stream measurement plane, illustrating the position of the wing tip vortex, adapted from Heyes et al. (Heyes & Smith, 2005).*

Vortex Models

Figure **2.3** shows a visual representation of different vortex models. Here, the swirl velocity distribution in a viscous vortex core is illustrated (Bhagwat & Leishman, 2002). The Rankine vortex model uses the idea of solid-body-like rotation in the core and a free vortex away from this core. The Lamb-Oseen vortex is a solution to the one-dimensional Navier-Stokes equation, by using an axisymmetric solution for the swirl velocity with the assumption that axial and radial velocities are zero. The Vatistas and Scully models are algebraic approximations of this Lamb-Oseen vortex (Bhagwat & Leishman, 2002).

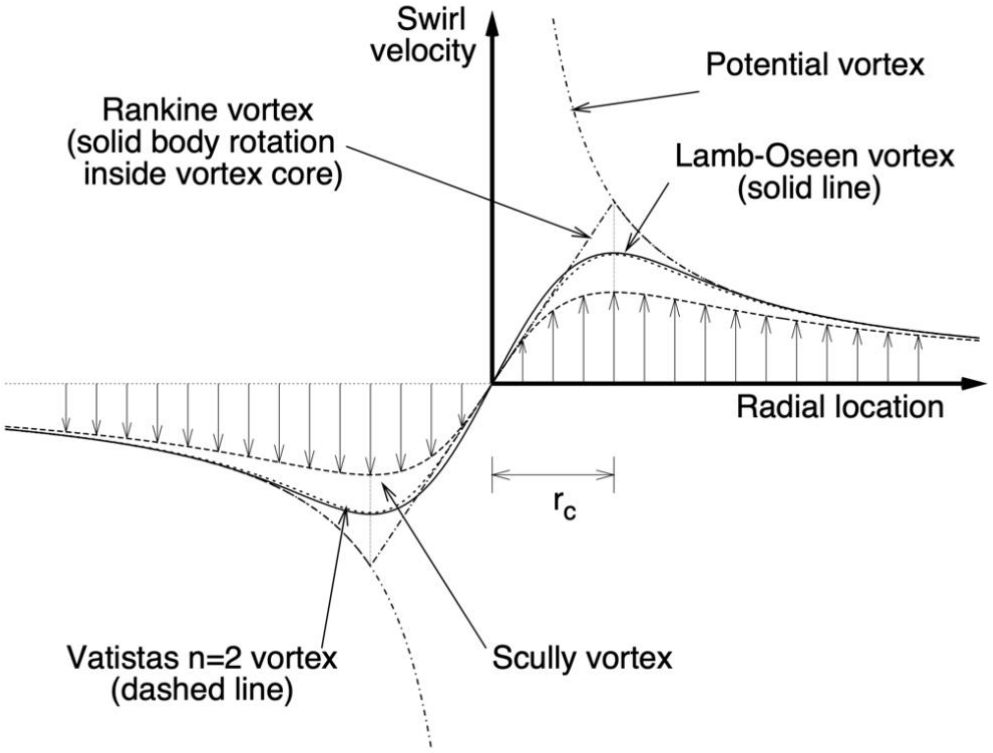

***Figure 2.3**: Distribution of induced swirl velocity inside a viscous vortex core on the basis of several models (Bhagwat & Leishman, 2002).*

The relation between its solid-body-like rotation near the vortex center and the free (potential) vortex further away can be found in Equation (2.1) (Bhagwat & Leishman, 2002). Here is U_θ the vortex-induced tangential velocity, Γ the net vortex circulation, and $\bar{r} = r/r_c$ the non-dimensional radial location, normalized by the viscous core radius, r_c. Given this model, it can be concluded that the vortex core radius can be determined as the distance from the center of the vortex to the location of the tangential velocity peak.

$$U_\theta(\bar{r}) = \begin{cases} \left(\frac{\Gamma}{2\pi r_c}\right)\bar{r}, & 0 \le \bar{r} \le 1, \\ \left(\frac{\Gamma}{2\pi r_c}\right)\frac{1}{\bar{r}}, & \bar{r} > 1 \end{cases} \qquad (2.1)$$

The Rankine model uses the circulation also known as the strength of the vortex, which is dependent on the vorticity, $\boldsymbol{\omega}$, see Equation (2.2). Vorticity is calculated by taking the curl of the velocity vector field, i.e., an analysis to determine the

rotation of particles around a certain axis. As Equation (2.2) shows, the circulation is calculated by taking the flux of the vorticity through a certain area A.

$$\Gamma = \iint_A \boldsymbol{\omega} \cdot \boldsymbol{n}\, dA \qquad (2.2)$$

Vortex Detection Methods

For isolated vortices, a peak in streamwise vorticity and the minimum and maximum of the tangential velocity will indicate the location of a vortex. However, for more complex problems, it is recommended to use the definition proposed by Jeong and Hussain, which states that the vortex core must have net vorticity, thus net circulation, and its geometry must be Galilean invariant (Jeong & Hussain, 1995). There are vortex detection methods, such as the Q-, λ_2-, and Γ_2- criterion (Günther & Theisel, 2018).

The Q-criterion describes the difference between the strain rate tensor and the vorticity tensor, see Equation (2.3) (Günther & Theisel, 2018). Here, $\boldsymbol{S}$ and $\boldsymbol{\Omega}$ represent the symmetric and the antisymmetric components of the velocity gradient tensor and represent the strain rate tensor and the vorticity tensor, respectively. The Q-criterion considers a vortex if the vorticity tensor is stronger than the strain rate tensor, such that $Q > 0$ (Günther & Theisel, 2018).

$$Q \equiv \frac{1}{2}\left(||\boldsymbol{\Omega}||^2 - ||\boldsymbol{S}||^2\right) \qquad (2.3)$$

The λ_2-criterion is a variation of the second invariant of the velocity gradient tensor and the pressure-minimum requirement, see Equation (2.4) (Jeong & Hussain, 1995).

$$\boldsymbol{S}^2 + \boldsymbol{\Omega}^2 = -\frac{1}{\rho}\nabla(\nabla p) \qquad (2.4)$$

Here represents $\nabla(\nabla p)$ the so-called Hessian matrix of the pressure. If there is a pressure minimum in a plane, the Hessian has two positive eigenvalues (Jeong & Hussain, 1995; Günther & Theisel, 2018). Following the equation, if $\boldsymbol{S}^2 + \boldsymbol{\Omega}^2$ has 3 eigenvalues, $\lambda_1 \geq \lambda_2 \geq \lambda_3$, a vortex is identified when λ_2 is negative. This is formulated as the criterion in Equation (2.5).

$$\lambda_2(\boldsymbol{S}^2 + \boldsymbol{\Omega}^2) < 0 \qquad (2.5)$$

In short, the Q-criterion determines areas in which the vorticity tensor dominates the strain rate tensor, whereas λ_2 gives the specific plane for the vortex region.

However, λ_2 neglects unsteady straining and viscous terms and is unsuitable for compressible flows. Furthermore, both the Q- and λ_2-criterion are based on the velocity gradient tensor, which could emphasize uncertainties in the flow.

Contrary to Q- and λ_2-criterion, Γ_2 does not use velocity gradients. It is based on the circulation of the vortex, evaluated in two dimensions at point $\boldsymbol{x}$ with a rectangular area, S, around it, see Figure **2.4** (Graftieaux, Michard, & Grosjean, 2001; Günther & Theisel, 2018). The area S is sampled with points $\boldsymbol{y}$ and defined as Equation (2.6). The method identifies a vortex core when Γ_2 goes up towards 1, as that identifies whether the flow goes around $\boldsymbol{x}$ by averaging the sine of the angle between the flow direction at $\boldsymbol{y}$ and the direction toward the sampled point $\boldsymbol{y}$ inside region S.

$$\Gamma_2(\boldsymbol{x}) = \frac{1}{|S|}\int_{\boldsymbol{y}\in S}\sqrt{1-\left(\frac{\left(\boldsymbol{v}(\boldsymbol{y})-\boldsymbol{v}_{avg}(\boldsymbol{y})\right)^T(\boldsymbol{y}-\boldsymbol{x})}{\left\|\boldsymbol{v}(\boldsymbol{y})-\boldsymbol{v}_{avg}(\boldsymbol{y})\right\|\cdot\|\boldsymbol{y}-\boldsymbol{x}\|}\right)^2}\,dS \qquad (2.6)$$

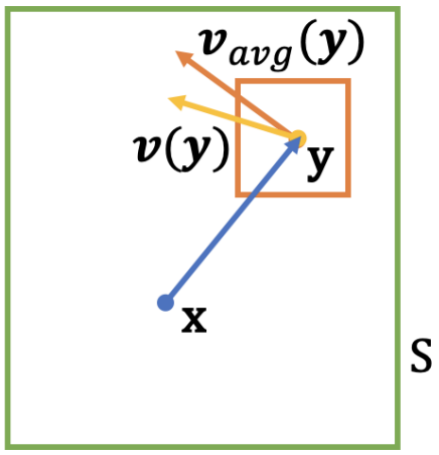

***Figure 2.4**: Visual representation of the Γ_2 − criterion.*

2.2 Vortex Breakdown

Figure **2.5** shows smoke visualization of vortex breakdown on the NASA High Alpha Research Vehicle project (Massey & Kandil, 1998). The upstream, steady part of the vortex and the downstream, unsteady part can be recognized by the diffusivity of the smoke. This point of transition between these states is often referred to as vortex breakdown (Mitchell & Délery, 2001). Vortex breakdown can be recognized by a sudden expansion of the vortex core and by a highly fluctuating structure downstream. As the angular momentum is preserved, the maximum value of the tangential velocity will decrease when the vortex grows in size. As this value decreases, the vorticity will decrease as well.

Figure 2.5: *Tuft and smoke visualization around the F/A-18 in the NASA High Alpha Research Vehicle project (Massey & Kandil, 1998).*

According to some researchers, the definition of turbulence should read as: *'Turbulence is "chaotic vorticity"'* (Nieuwstadt, Boersma, & Westerweel, 2016). Equation (2.7) is derived from the Navier-Stokes equations and represents the change in vorticity when moving along a fluid element (Nieuwstadt, Boersma, & Westerweel, 2016). The first term on the right-hand side represents the rate-of-strain tensor. This describes the interaction between fluid deformation and vorticity production. The deformation is divided between the tilting and stretching of the vortex vector. The second term of the right-hand side describes the diffusion

of the vorticity due to viscosity. As the vortex stretches, the vorticity increases such that the vortex will become unstable. The structure then disintegrates into smaller structures, which is known as vortex breakdown (Nieuwstadt, Boersma, & Westerweel, 2016).

$$\frac{D\omega_i}{Dt} \equiv \frac{\partial \omega_i}{\partial t} + u_j \frac{\partial \omega_i}{\partial x_j} = \omega_j \frac{\partial u_i}{\partial x_j} + \nu \frac{\partial^2 \omega_i}{\partial x_j^2} \qquad (2.7)$$

Previous Research

After the publication of a study in the mid-1950s where an observation was made of a condensation trail 'belling-out' before disappearing, the topic of vortex breakdown became popular to research (Peckham & Atkinson, 1957). Previous research focused on whether breakdown affected the aerodynamic properties of a delta wing as well as research into the dynamics of vortex breakdown itself (Escusier, 1988). Sarpkaya studied the range of breakdown patterns and the effect of an adverse pressure gradient on the position of vortex breakdown (Sarpkaya, On Stationary and Travelling Vortex Breakdowns, 1971; Sarpkaya, Vortex Breakdown in Swirling Conical Flows, 1971; Sarpkaya, Effect of the Adverse Pressure Gradient on Vortex Breakdown, 1974). According to these studies, there are many types of vortex breakdown, but Sarpkaya proposed the main three types depicted in Figure **2.6**. These are, top to bottom, the so-called double helix, spiral, and bubble type of vortex breakdown (Délery, 1994).

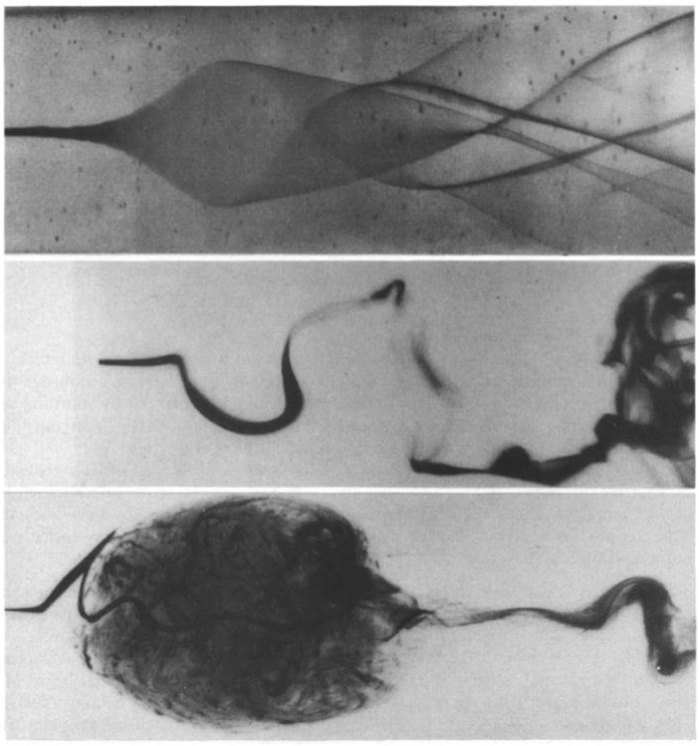

Figure 2.6: *Various types of vortex breakdown: helix (top), spiral (middle), and bubble (bottom). The flow direction is from left to right. (Sarpkaya, Vortex Breakdown in Swirling Conical Flows, 1971).*

The relation between other flow properties and the occurrence of breakdown has been investigated by Sarpkaya in the 1970s. In the study published in 1974, it was hypothesized that the upstream movement of the breakdown location should be the result of an adverse pressure gradient, as well as the Reynolds number and the circulation (Sarpkaya, Effect of the Adverse Pressure Gradient on Vortex Breakdown, 1974).

To validate this statement, experiments were performed using the experimental set-up depicted in Figure **2.7**. Here, the swirl of the vortex was supplied by the rotation of 32 streamlines foils that were placed around the inlet. The flow rate was controlled by a valve and flow meters downstream of the tube. The vortex, and its breakdown, were visualized by ink. The pressure gradient was altered by changing the divergence angle of the test section.

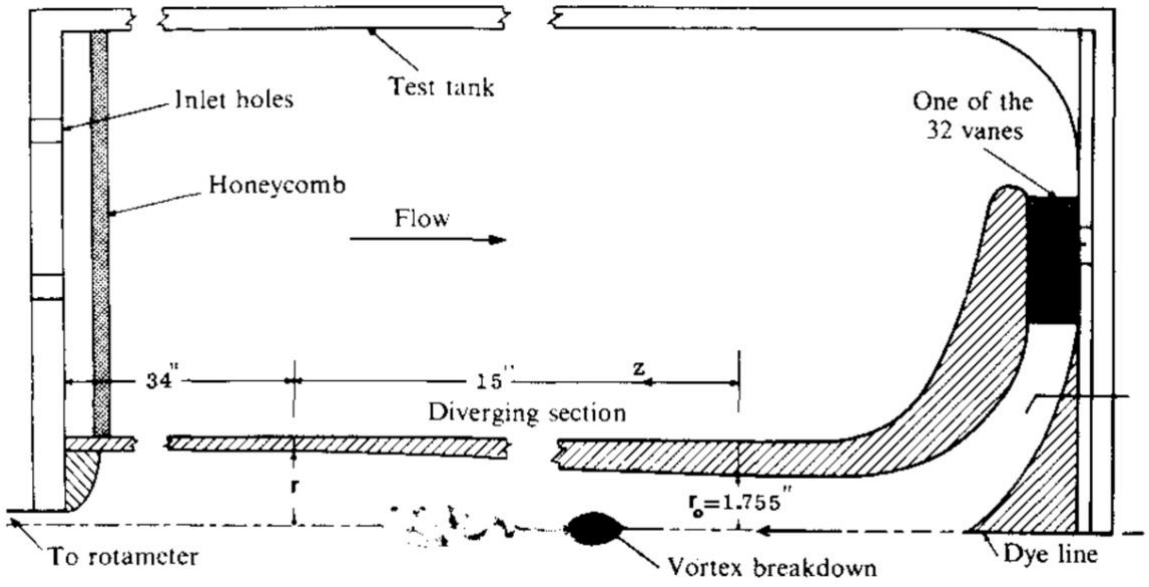

***Figure 2.7**: Top half of experimental set-up of Sarpkaya (Sarpkaya, Effect of the Adverse Pressure Gradient on Vortex Breakdown, 1974).*

Figure **2.8** shows the results of the experiments conducted by Sarpkaya. The relation between the degree of divergence (i.e., the adverse pressure gradient), the breakdown location of the vortex, and the Reynolds number for a constant normalized circulation ($\Omega = 1.0$) is shown with the dashed black lines. Here, the Reynolds number is defined as $Re = \overline{W_0} D_0/\nu$, where $\overline{W_0}$ is the mean velocity at $z = 0$, D_0 the minimum tube diameter, and ν the kinematic viscosity. Figure **2.9** illustrates the results for a constant pressure gradient, but different values of circulation. The normalized circulation is defined as $\Omega = \Gamma/\overline{W_0} D_0$, where Γ is the circulation imparted to the flow.

From the data in Figure **2.8** it can be concluded that the breakdown location moves upstream at a constant Reynolds number for the two tubes with the smallest divergence angle. However, this relation is not true for the two largest angles of divergence. Sarpkaya stated this behavior as a consequence of the limitations of the experiment (Sarpkaya, Effect of the Adverse Pressure Gradient on Vortex Breakdown, 1974). The flow along the diverging walls was separated and reversed and thus interfering with the vortex breakdown.

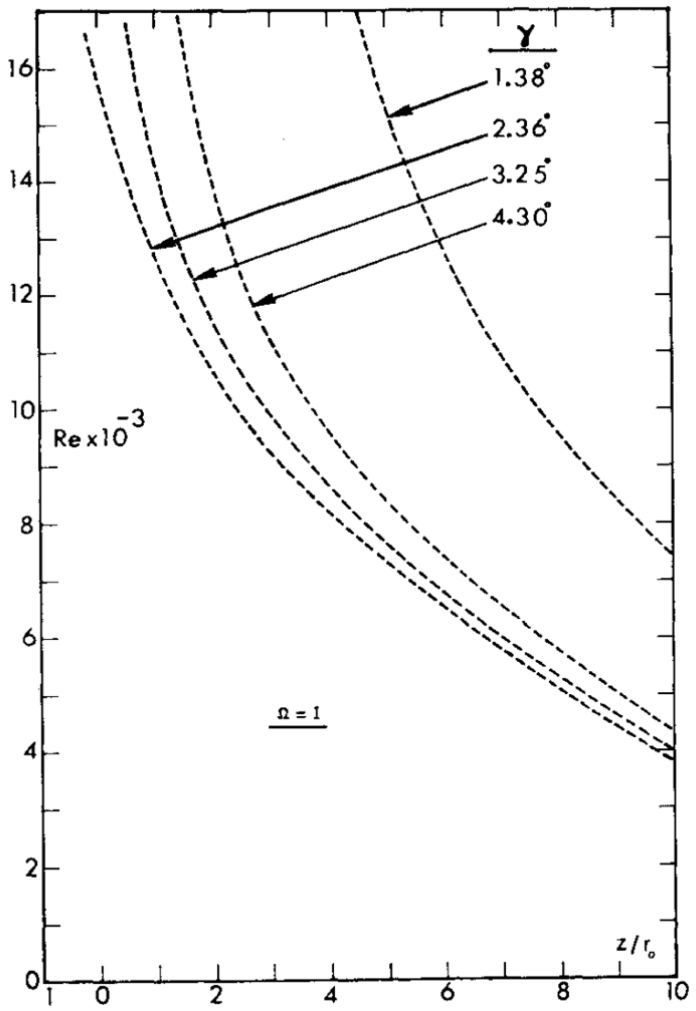

***Figure 2.8**: Breakdown location as a function of Reynolds for various angles of divergence and normalized circulation equals 1.0 (Sarpkaya, Effect of the Adverse Pressure Gradient on Vortex Breakdown, 1974).*

The data in Figure **2.9** shows that the breakdown location, at constant circulation, moves upstream for a higher Reynolds number. This is similar to boundary layer transition. Also, the breakdown location moves upstream for a constant Reynolds number, but increasing circulation. The increase in circulation is linked to an increase in vorticity. This increase will ensure earlier breakdown into smaller structures, hence the upstream movement. The conclusion of the paper was that even though the pressure gradient is of great influence, other flow parameters also influence the breakdown location (Sarpkaya, Effect of the Adverse Pressure Gradient on Vortex Breakdown, 1974).

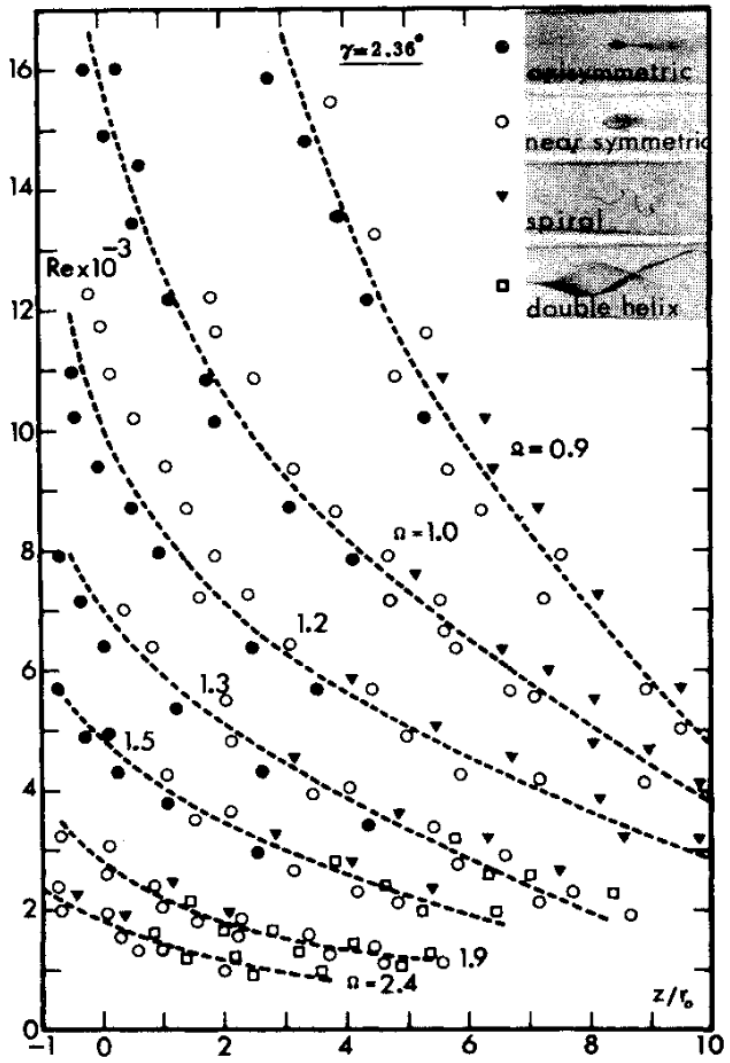

Figure 2.9: Relation between vortex breakdown at constant pressure gradient and Reynolds number and normalized circulation (Sarpkaya, Effect of the Adverse Pressure Gradient on Vortex Breakdown, 1974).

3. Particle Image Velocimetry

Vortex breakdown is a turbulent phenomenon, thus techniques able to reconstruct three-dimensional flow fields from experimental data are discussed. Particle Image Velocimetry (PIV) is widely used and, over time, adapted to capture a three-dimensional flow field. First, the working principle of PIV will be elaborated upon. After which, three-dimensional PIV, or Tomographic PIV (Tomo-PIV), will be discussed. Then, the combination of the Coaxial Volumetric Velocimeter (CVV) and Shake-The-Box (STB), which is a Lagrangian Particle Tracking (LPT) technique will be discussed. This combination of CVV with LPT is also known as robotic volumetric PIV.

Working principle of PIV

PIV can estimate the kinematics of a flow field using a system of seeding particles, laser illumination, and digital imaging (Grant, 1997). Figure **3.1** illustrates its working principle. The flow field gets seeded by tracer particles, which are imaged by taking an image pair of which the second image is taken rapidly after the first one. In the subsequent step is the image divided into small interrogation windows. The local displacement vector of such window is determined by a cross-correlation algorithm (Raffel, et al., 2018). By using the displacement and the time interval, the velocity vector is determined for each window. This evaluation is repeated for the entire area of the PIV recording.

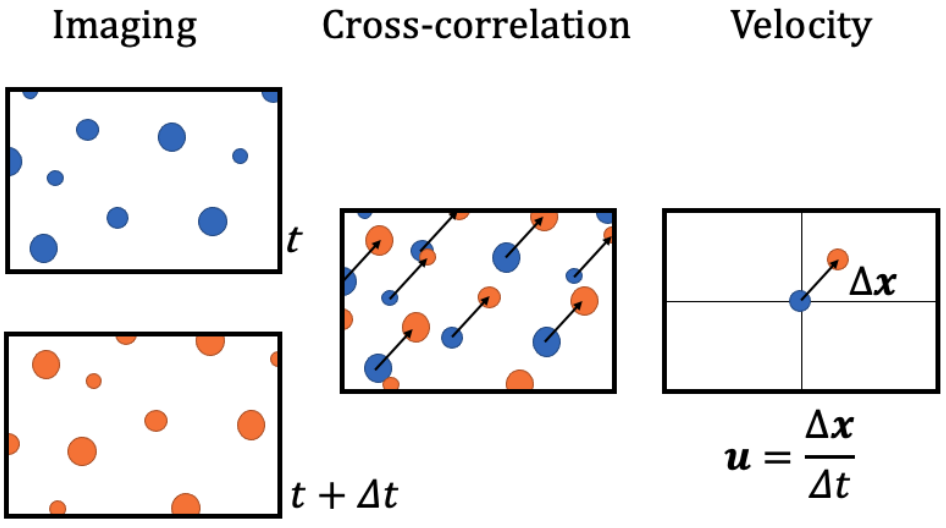

***Figure 3.1**: Visual representation of the PIV working principle.*

By means of different set-ups of the imaging systems, different flow fields can be reconstructed. A single camera perpendicular to a laser sheet (planar PIV) will allow for a two-dimensional flow field of two velocity components. Two cameras (stereoscopic PIV) can reconstruct a two-dimensional flow field in three velocity components. Three or more cameras (Tomo-PIV) can reconstruct the flow field in three dimensions and three velocity components.

3.1 Three-Dimensional PIV

Working Principle of Tomo-PIV

Figure **3.2** illustrates the working principle of Tomo-PIV. The flow field gets reconstructed from recordings taken simultaneously from multiple viewing directions (Elsinga, Scarano, Wieneke, & van Oudheusden, 2006). For these recordings, the tracer particles must be visible and in focus throughout the measurement volume. Therefore, the focal depth has to match the depth of the measurement volume (Scarano, 2013). This depth is obtained by expanding the thickness of the light sheet. Similar to two-dimensional PIV, the particles must be able to follow the flow closely to give an accurate estimation of the flow field. The particles must also be seeded homogeneously throughout the field.

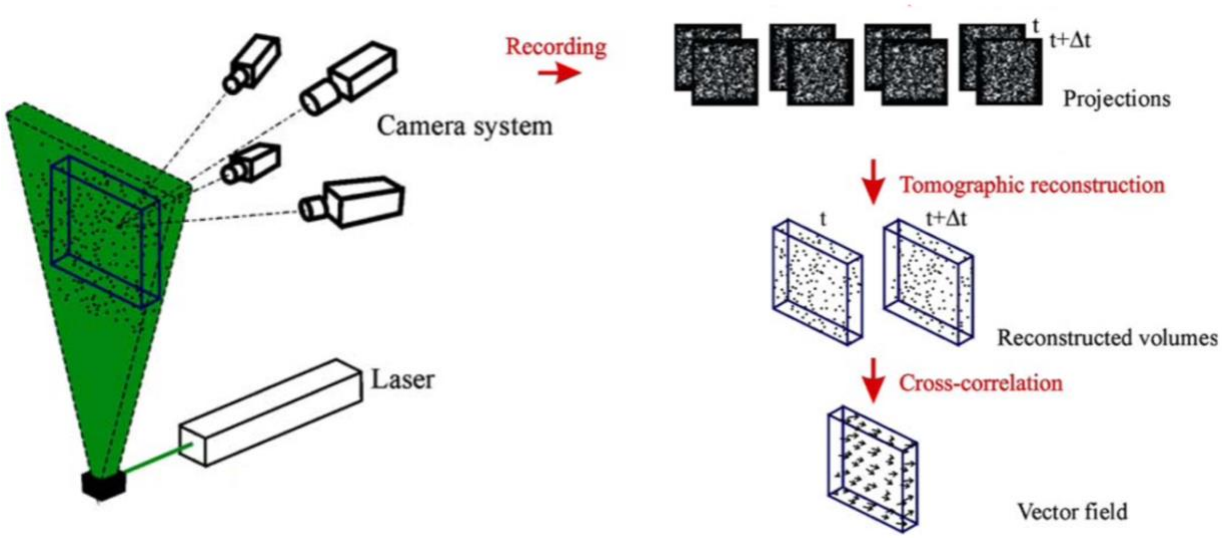

***Figure 3.2**: Working principle Tomo-PIV, adapted from Elsinga et al. (Elsinga, Scarano, Wieneke, & van Oudheusden, 2006).*

The configuration of the camera system determines the tomographic aperture, β. As Figure **3.3** illustrates, the particle position accuracy in the depth direction of the cameras is dependent on this aperture. The accuracy of the position decreases with decreasing β (Scarano, 2013).

From the recordings, the images get processed in two steps. First, the flow field is discretized into cubic voxel elements. Then, the data is processed using a cross-correlation algorithm. This step is similar to two-dimensional PIV, albeit extended from pixel to voxel-based objects (Elsinga, Scarano, Wieneke, & van Oudheusden, 2006).

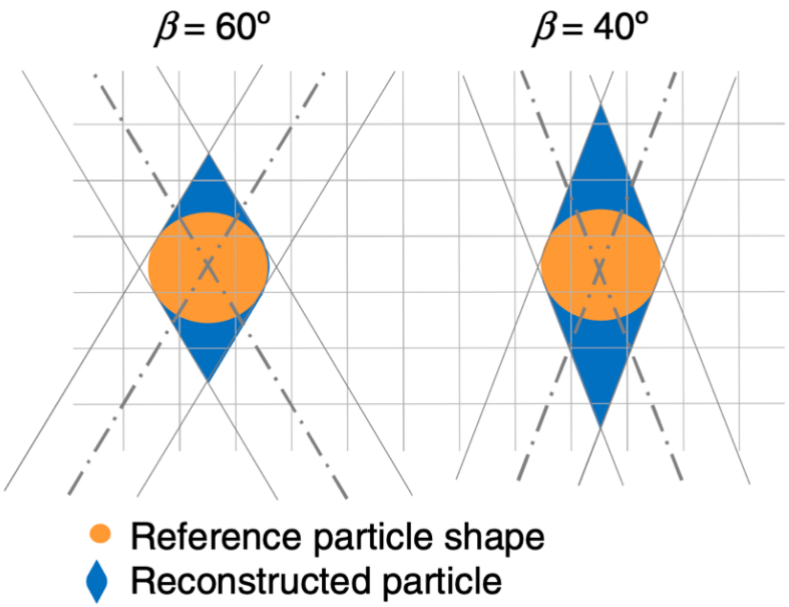

***Figure 3.3**: Tomo-PIV particle reconstruction (Scarano, 2013).*

Applications of Tomo-PIV

The research of Wang et al. uses qualitative flow visualization to identify the breakdown phenomenon, capture the breakdown position, and the type of breakdown, before applying Tomo-PIV processing (Wang, Gao, Wei, Li, & Wang, 2016). The experimental set-up for this study into vortex breakdown over a non-slender delta wing is shown Figure **3.4**, and a visualization of the measurement volume can be found in Figure **3.5**. As part of data processing, dye streams are separated from the particle traces and are processed separately. These streaklines are reconstructed using a multiplicative algebraic reconstruction technique algorithm and the particle traces went through a traditional Tomo-PIV process (Wang, Gao, Wei, Li, & Wang, 2016).

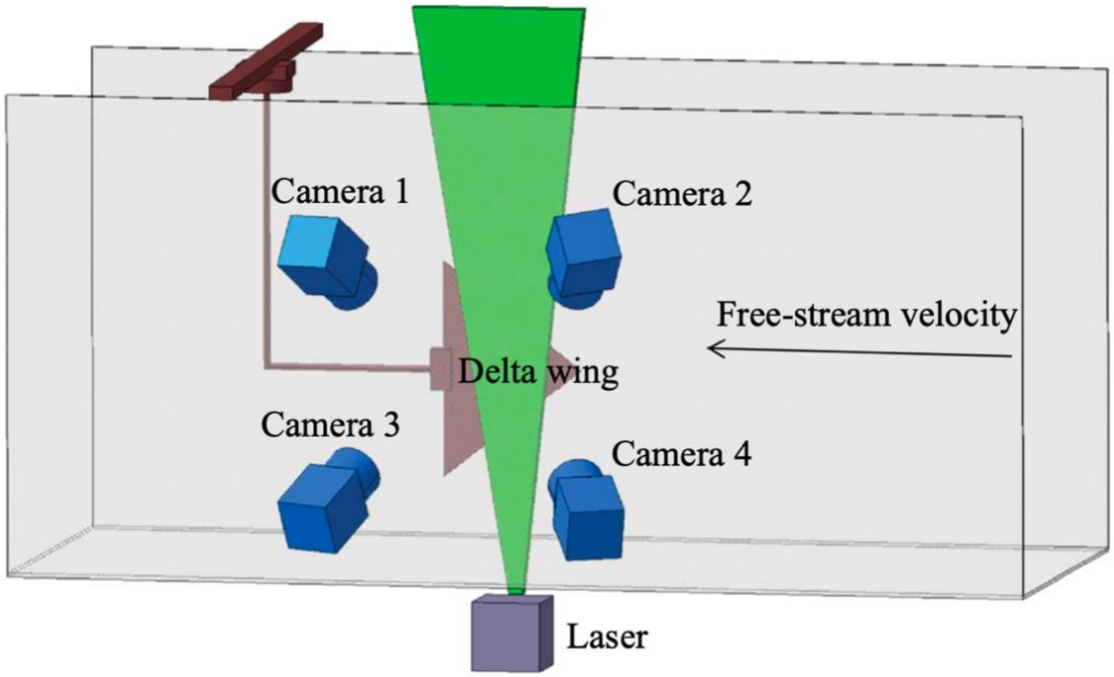

***Figure 3.4**: Experimental set-up Wang et al. (Wang, Gao, Wei, Li, & Wang, 2016).*

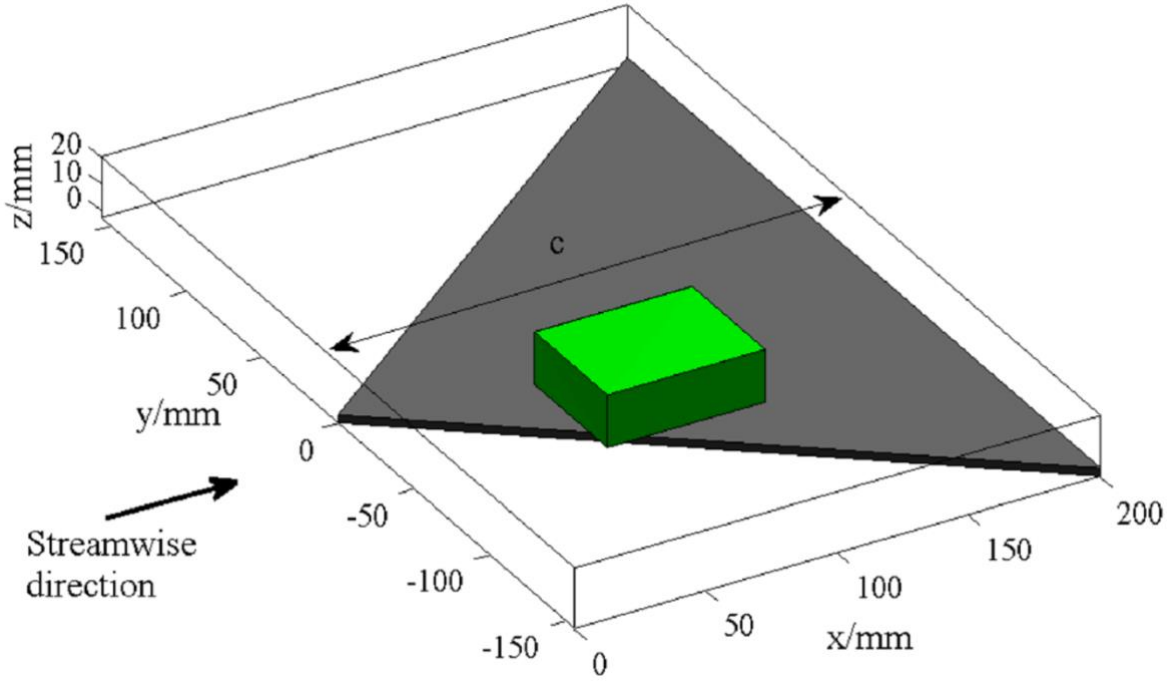

***Figure 3.5**: Measurement volume in experiment of Wang et al. (Wang, Gao, Wei, Li, & Wang, 2016).*

Figure **3.6** illustrates a time-averaged velocity field. The vortex can be located intuitively from the vectors and the velocity deficit on the planes. To confirm the location of this vortex, a comparison between the dye streakline data and the Tomo-PIV data is presented. Figure **3.7** shows the reconstructed dye streakline on the left and the Tomo-PIV data on the right. The Q-criterion is applied to the Tomo-PIV data to identify the vortex more accurately. The study concludes that the datasets compared well. Thus, Tomo-PIV is a suitable method for analyzing vortices and their breakdown, albeit time-consuming (Wang, Gao, Wei, Li, & Wang, 2016).

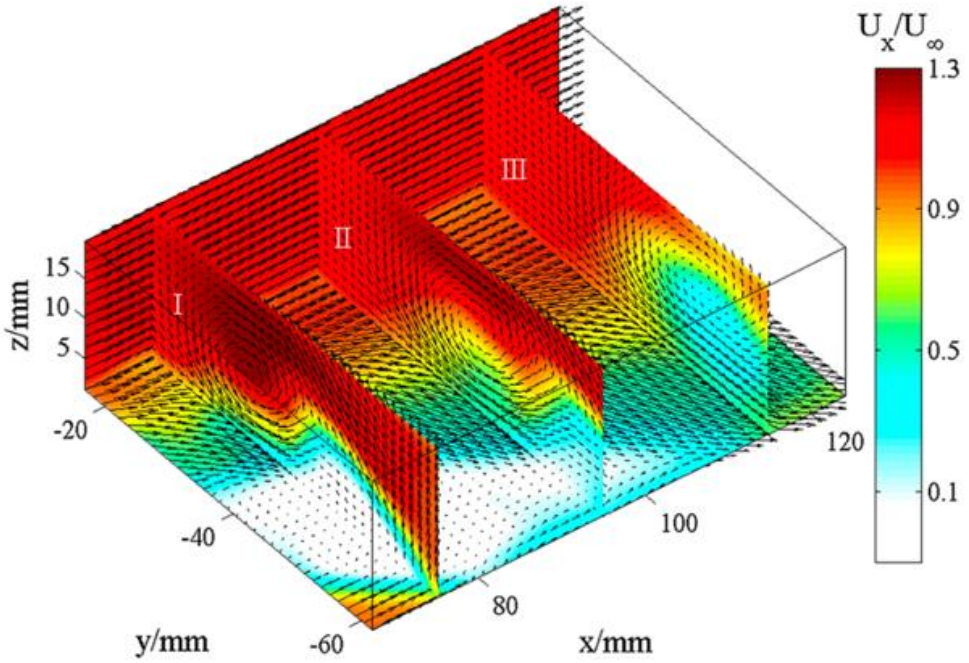

***Figure 3.6**: Time-averaged velocity field at three spanwise and plane-normal sections, and two edge sections, adapted from Wang et al. (Wang, Gao, Wei, Li, & Wang, 2016)*

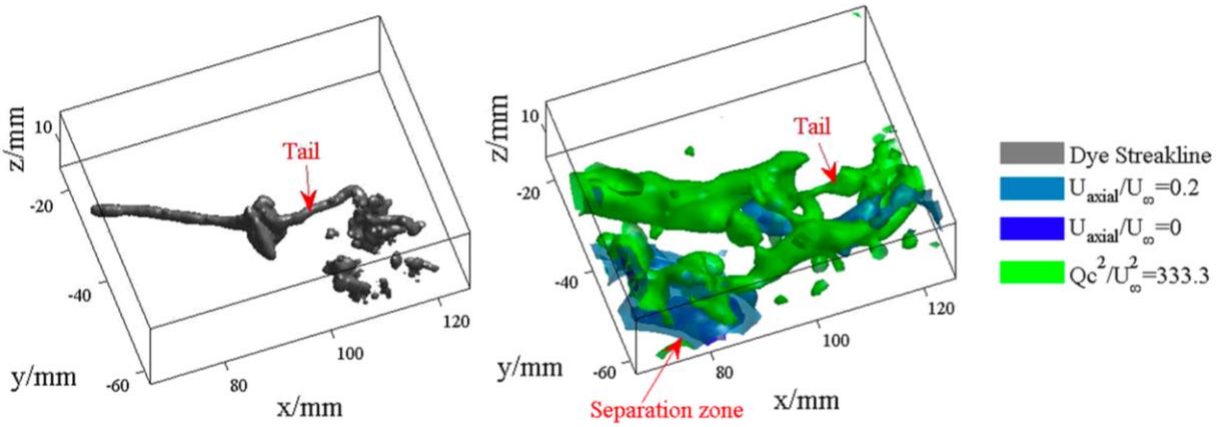

***Figure 3.7**: Visualization of bubble-type vortex breakdown using iso-surface of dye streakline (left) and iso-surface using the Q-criterion (right), adapted from Wang et al. (Wang, Gao, Wei, Li, & Wang, 2016).*

Limitations of Tomo-PIV

Even though Tomo-PIV has experienced huge success since its introduction, there are some drawbacks. For example, as the method applies spatial averaging in the cross-correlation step, it smooths out velocity gradients in fine flow structures (Schanz, Gesemann, & Schröder, 2016). Despite the successful results of Wang et al., this indicates that Tomo-PIV could potentially miss internal vortex dynamics. Also, it is unavoidable to introduce errors in the particle position accuracy by discretization of the particles using a voxel space (Schanz, Gesemann, & Schröder, 2016). Furthermore, the method is (computationally) time-consuming and complex in its set-up (Schanz, Gesemann, & Schröder, 2016; Wang, Gao, Wei, Li, & Wang, 2016).

3.2 Robotic Volumetric PIV

Robotic volumetric PIV is a combination of using CVV and LPT. STB is often chosen as the LPT algorithm (Jux, Sciacchitano, Schneiders, & Scarano, 2018). CVV is a technique that was developed to, amongst other things, reduce the system size and optical access requirements of Tomo-PIV, making it more user-friendly. Figure **3.8** shows that CVV has its illumination and imaging system arranged coaxially. By doing so, the tomographic aperture is reduced by an order of magnitude (Schneiders, Scarano, Jux, & Sciacchitano, 2018).

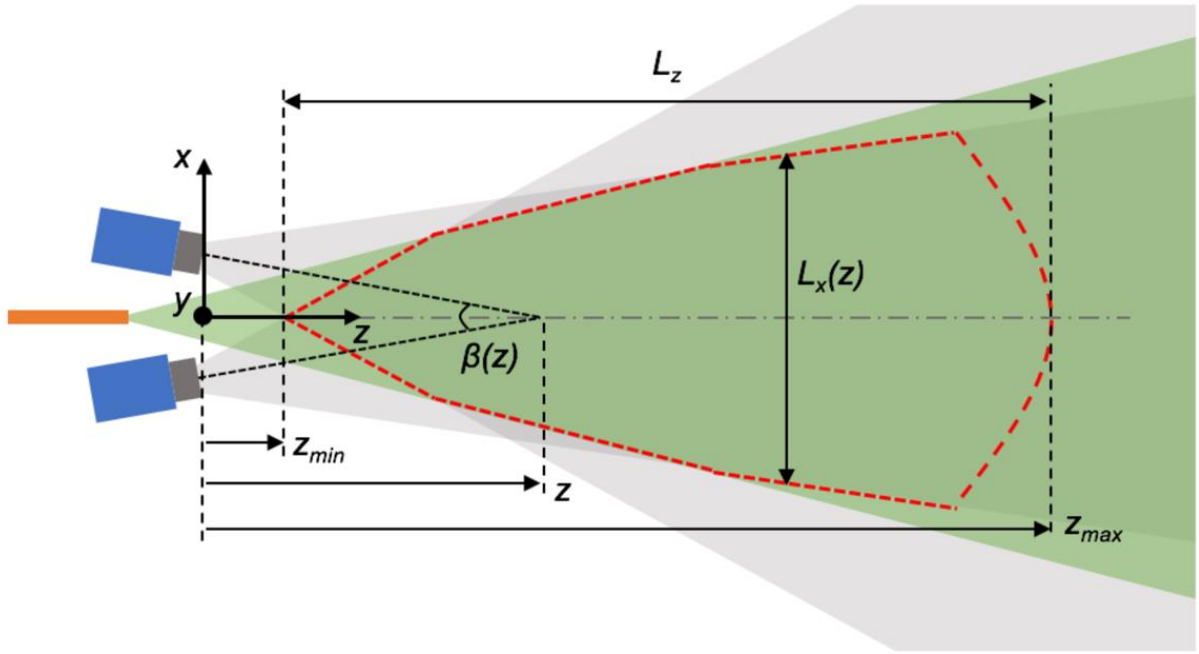

***Figure 3.8**: CVV set-up (Schneiders, Scarano, Jux, & Sciacchitano, 2018).*

Working Principle of Robotic Volumetric PIV

The working principle of robotic volumetric PIV appears similar, but differs from Tomo-PIV. Both rely on tracer particles, laser illumination, multiple cameras, and algorithms to reconstruct the velocity field. However, the main differences are based on the set-up and the data processing algorithms.

As the illumination and cameras are placed coaxially, the measurement volume has a greater depth than Tomo-PIV. This requires that the imaging aperture needs to be small such that all particles are in focus. However, this also reduces the light collected on the imager (Schneiders, Scarano, Jux, & Sciacchitano, 2018). It is therefore chosen to use particles of higher scattering efficiency, such as Helium Filled Soap Bubbles (HFSB). HSFB are naturally buoyant, which makes them suitable as tracer particles, and are bigger than typical oil droplets, thus providing a much higher scattering efficiency (Bosbach, Kühn, & Wagner, 2009). Note, that as the tomographic aperture is smaller than at Tomo-PIV, the positional accuracy of the particles in the depth direction decreases as well, see Figure **3.9** (Schneiders, Scarano, Jux, & Sciacchitano, 2018).

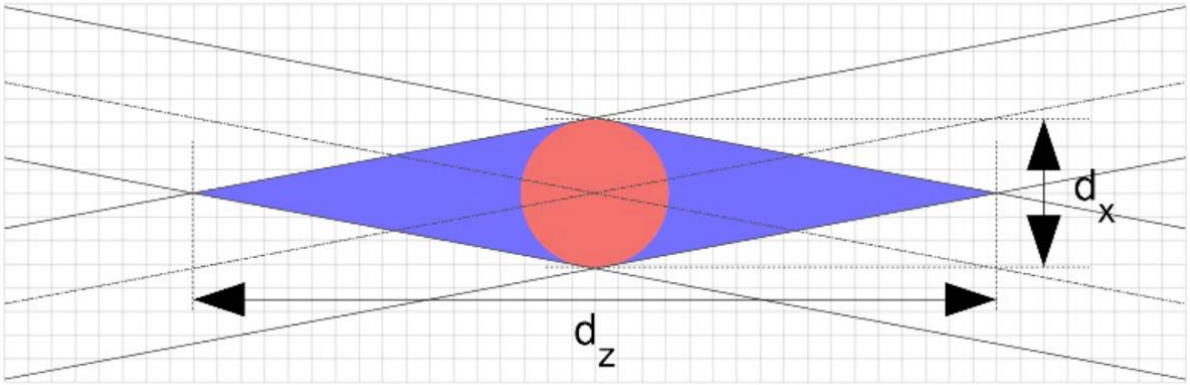

***Figure 3.9**: Reconstructed particle using CVV (Schneiders, Scarano, Jux, & Sciacchitano, 2018).*

To process the data, STB is used, which differs from Tomo-PIV data processing. Figure **3.10** shows a visual representation of the structure of the results of both algorithms. For Tomo-PIV, a tomographic reconstruction of each time step is done, after which cross-correlation is performed over the entire PIV area (Elsinga, Scarano, Wieneke, & van Oudheusden, 2006). Or, in other words, it determines the particle distribution first, after which the velocity is determined. STB uses the available velocity information to estimate a particle distribution first, after which it uses this information to support the reconstruction process of the particle trajectories (Schanz, Gesemann, & Schröder, 2016). This estimation of the particle location is done by 'shaking' the particle around in three-dimensional space until its local residual is minimized (Wieneke, 2013). The resulting flow field contains a vector for each particle. To organize such unstructured data, the results of STB are binned and structured onto a cartesian grid.

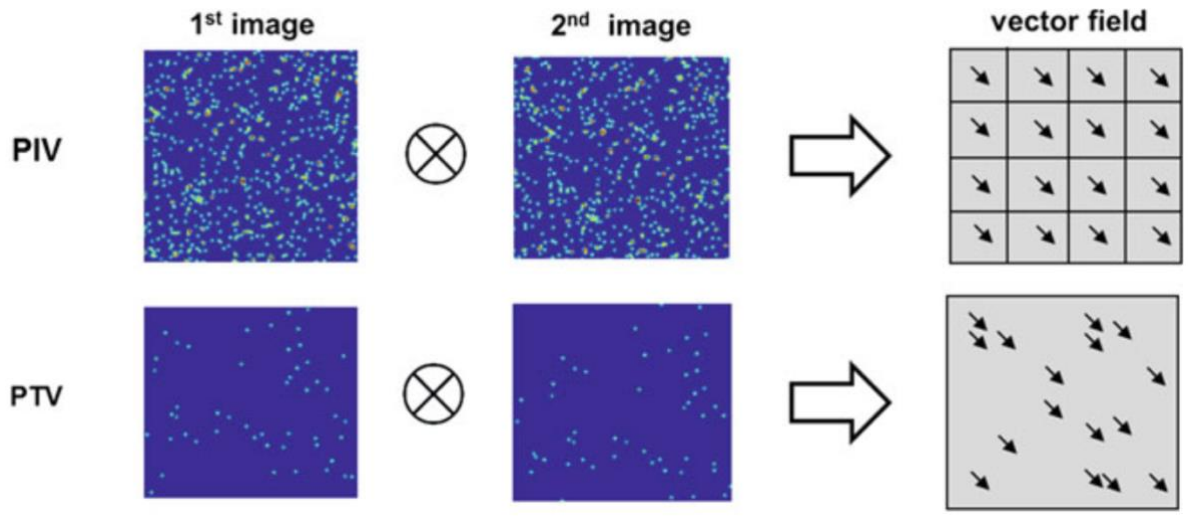

***Figure 3.10**: Difference between PIV and particle tracking velocimetry processing, adapted from Raffel et al. (Raffel, et al., 2018).*

Applications of Robotic Volumetric PIV

There are several applications of robotic volumetric PIV (Jux, Sciacchitano, Schneiders, & Scarano, 2018; Schneiders, Scarano, Jux, & Sciacchitano, 2018; Jux, Scarano, & Sciacchitano, 2019). One of these studies used a full-scale reproduction of a professional cyclist to measure large-scale complex aerodynamic structures. Here, the experimental set-up of Figure **3.11** was used. HFSB were used as tracer particles, the CVV set-up, a robot arm with six degrees of freedom, and STB were used.

The motion of the particle tracers was obtained by STB coupled to their location using robotic CVV (Jux, Sciacchitano, Schneiders, & Scarano, 2018). In Figure **3.12** some processed results are shown, here the contours of the streamwise vorticity, ω_z, can be found for $z = 10$ mm, which is combined with iso-surfaces of $\omega_z = \pm 100\ \mathrm{s}^{-1}$. The study by Jux et al. concluded that the flow topology compared well to the available literature (Jux, Sciacchitano, Schneiders, & Scarano, 2018).

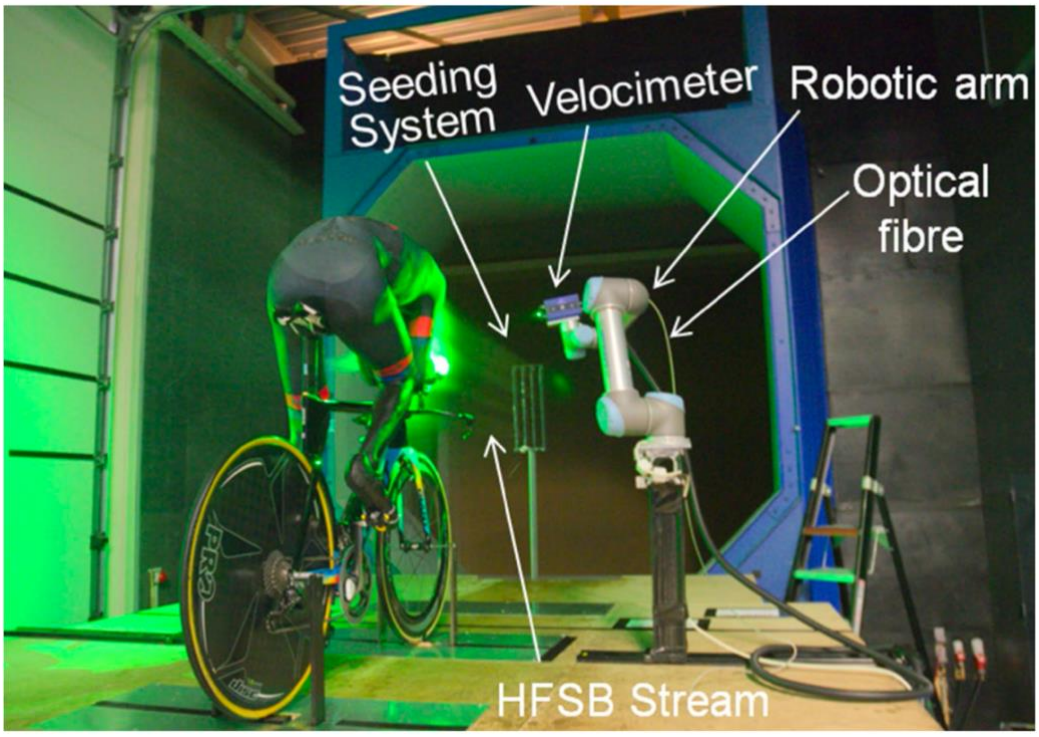

***Figure 3.11**: Set-up CVV experiment (Jux, Sciacchitano, Schneiders, & Scarano, 2018).*

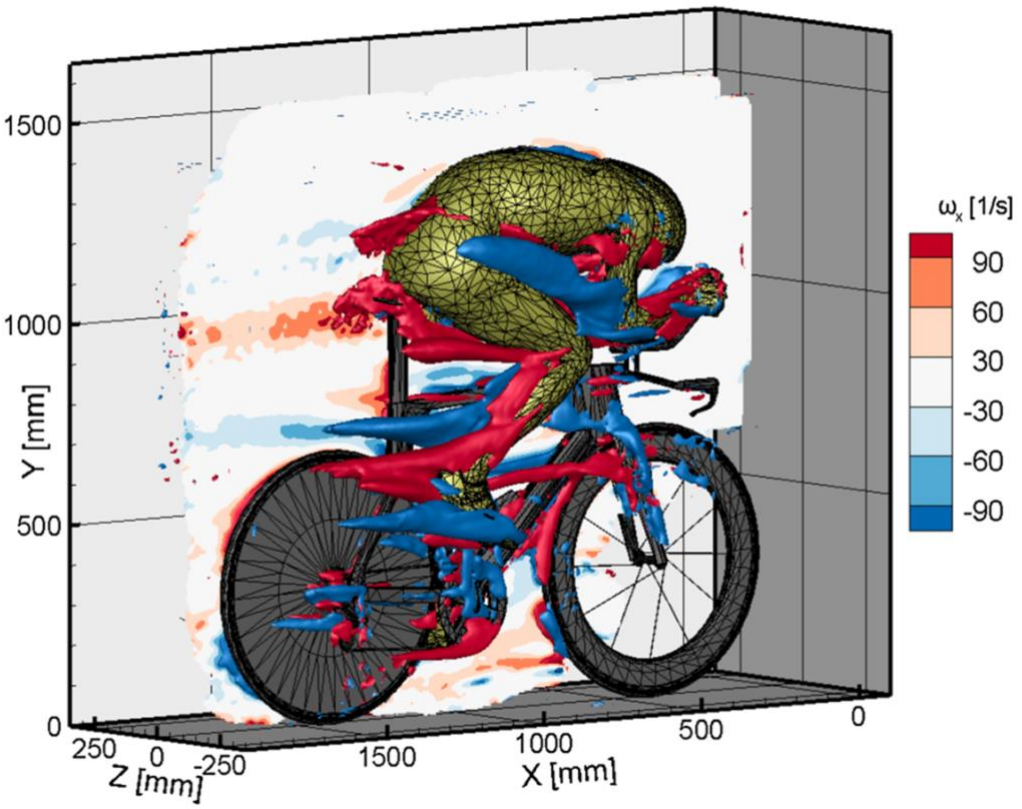

***Figure 3.12**: Flow topology of vorticity obtained with CVV and STB (Jux, Sciacchitano, Schneiders, & Scarano, 2018).*

4. Methodology

The methodology of the experimental campaign of this thesis is elaborated upon. First, the experimental set-up is described, after which the vortex identification method is discussed. Then, the estimation of the vortex breakdown location and the definition of some local flow properties is presented.

4.1 Experimental Set-Up

To be able to assess the feasibility of measuring a free, streamwise vortex and its breakdown using robotic volumetric PIV, whilst analyzing the relation between local flow properties and the location of the breakdown, an experimental study was performed. The W-Tunnel at the TU Delft High-Speed Lab was used. This tunnel is an open, low-speed wind tunnel, with a square, exchangeable exit. The inlet of the tunnel consists of a plenum with dimensions 2.0 m x 1.5 m x 2.0 m. The air passes through the diffuser which decelerates the flow, the settling chamber with two gauzes to diminish the turbulence intensity, the contraction with accelerates the flow, and finally the nozzle where the air is blown into the free atmosphere. The nozzle exit has a cross-section of 0.60 m x 0.60 m. With this exit configuration is the maximum velocity around 15 m/s and can be regulated by setting the revolutions per minute of the centrifugal fan. The turbulence intensity of the W-Tunnel is approximately 0.5%.

Figure **4.1** shows a picture of the set-up used during the experimental campaign with labels indicating the components. Figure **4.2** shows a schematic of the set-up where the cylinder was placed at $x_{cyl} = 75$ cm. Here, it is illustrated that the vortex was generated as the tip vortex of a half-span wing. In the top view of Figure **4.2**, the pressure field generated by the cylinder is illustrated as well. The colored lines indicate values for the pressure coefficient from 0 in dark blue, to 0.9 in red. The cylinder was 20 cm in diameter and 100 cm in length, such that it extended to the bottom and top of the test section. Furthermore, the angle of attack is indicated as α, and the location of the origin is shown at the trailing edge of the wing tip.

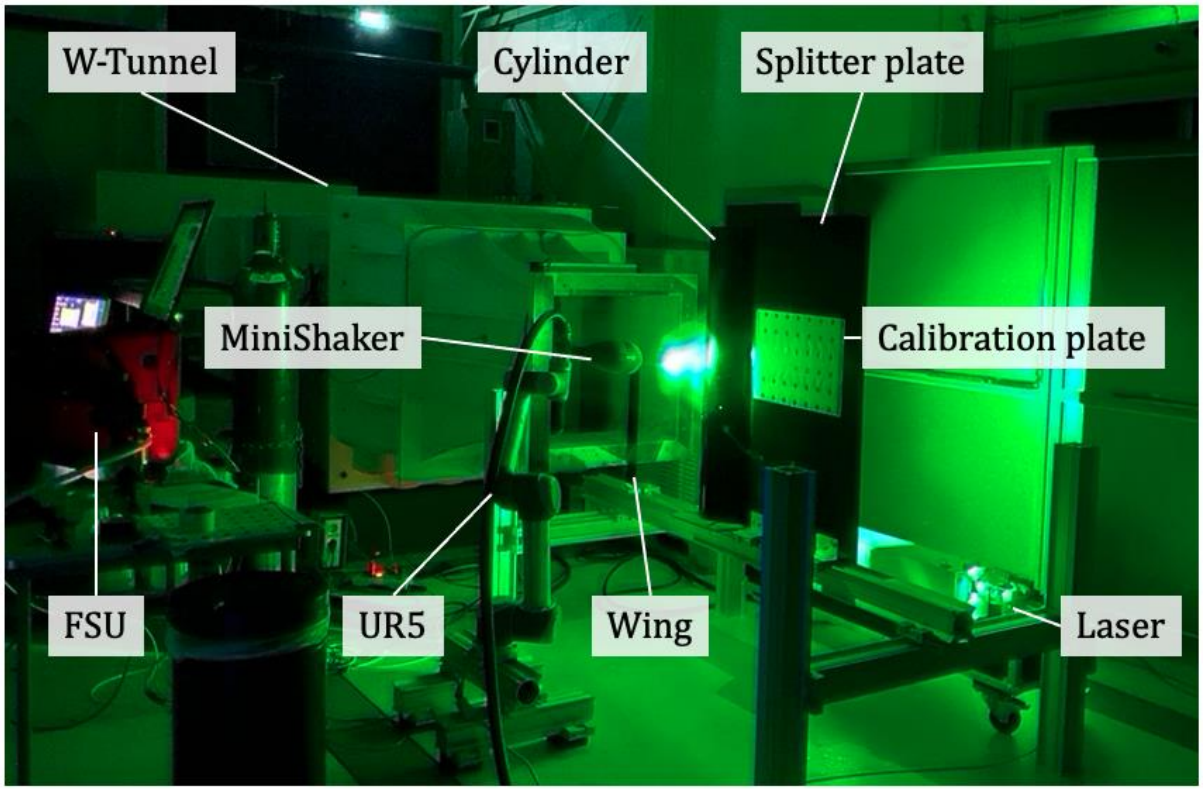

***Figure 4.1**: Picture of the experimental set-up.*

The wing was a flat-tip NACA0018 aluminum profile of 50 cm with a 12 cm chord, of which 30 cm was inserted in the flow field to ensure the vortex was propagating in the center of the test section. To avoid reflections of the laser illumination, the reflective surface of the profile was painted black. As can be seen from Figure **4.1**, behind the cylinder, a dark wood plate is attached to avoid vortex shedding of the cylinder and thus minimizing the upstream effect of the *Von Kármán Vortex Street*. All components are attached to clamps which can lock and slide over aluminum beams to change the cylinder distance, x_{cyl}, to 50 cm, 75 cm, and 100 cm. Tests were conducted at $U_\infty = 8$ m/s, 10 m/s, and 12 m/s.

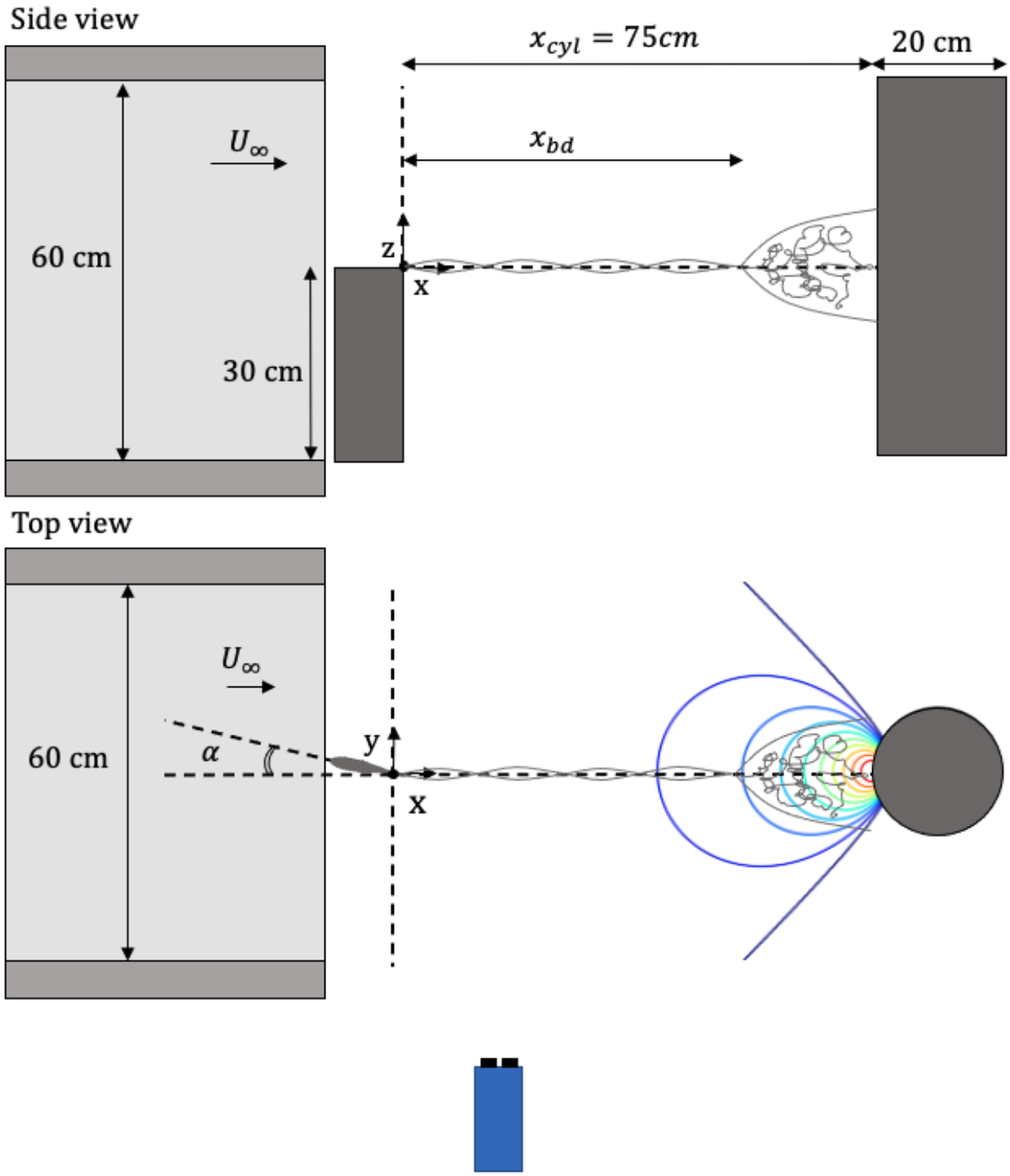

***Figure 4.2**: Schematic of the top and side view of the experimental set-up. A sketch of a vortex and its breakdown is included, as well as the isolines of the pressure coefficient from the pressure field generated by the cylinder.*

The HFSB are generated by a 10-wing, 200-nozzle rake which is installed in the settling chamber of the W-Tunnel. This rake is controlled by a homemade Fluid Supply Unit (FSU) regulating the mass flow of helium, air, and soap. One nozzle generates 20,000 – 60,000 bubbles per second and these bubbles are 300-500 µm in diameter (Jux, Scarano, & Sciacchitano, 2019).

The density of HFSB throughout the vortex core was controlled by changing the ratio of helium and soap. Figure **4.3** shows the trajectory of heavier-than-air (HTA) and lighter-than-air (LTA) tracers. HTA will lead to an empty vortex core and LTA bubbles will concentrate at the vortex axis (Caridi, Sciacchitano, & Scarano, 2017). See Figure **4.4** for a picture showcasing the effect of HTA bubbles and Figure **4.5** for LTA bubbles. The helium to soap ratio was qualitatively tweaked, but the vortex core remained visible due to a concentration of HFSB at the core, therefore, it is plausible that the vortex core was inhomogeneously seeded. The ratio of the mass flow rate of helium and soap was approximately 10^3:1, respectively (Faleiros, Tuinstra, Sciacchitano, & Scarano, 2019).

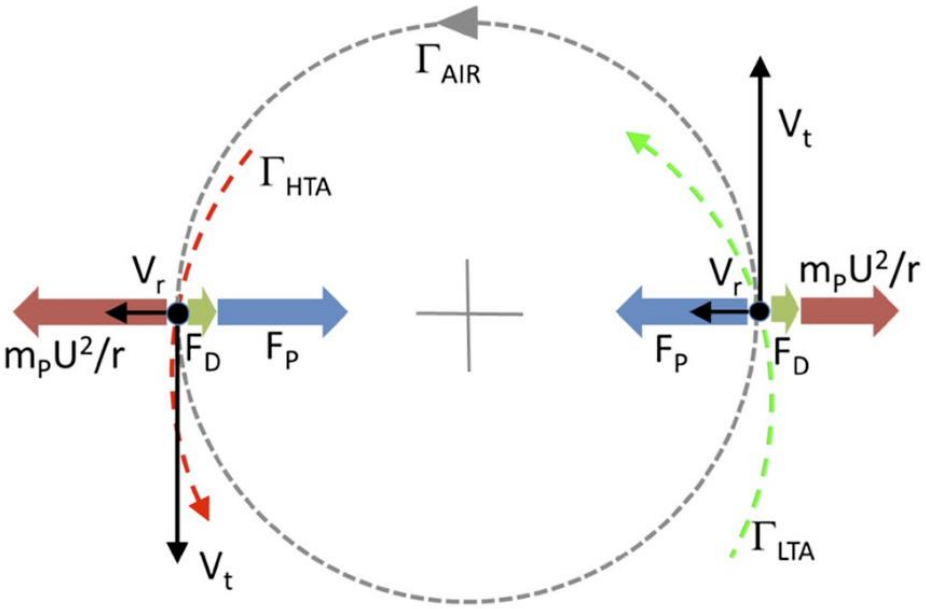

***Figure 4.3**: Trajectory of heavier-than-air (HTA) in red and lighter-than-air (LTA) in green for a circular motion of which the vectors are indicated in black (Caridi, Sciacchitano, & Scarano, 2017).*

Figure 4.4: *No vortex core visualization with HTA HFSB.The freestream direction is indicated with the white arrow.*

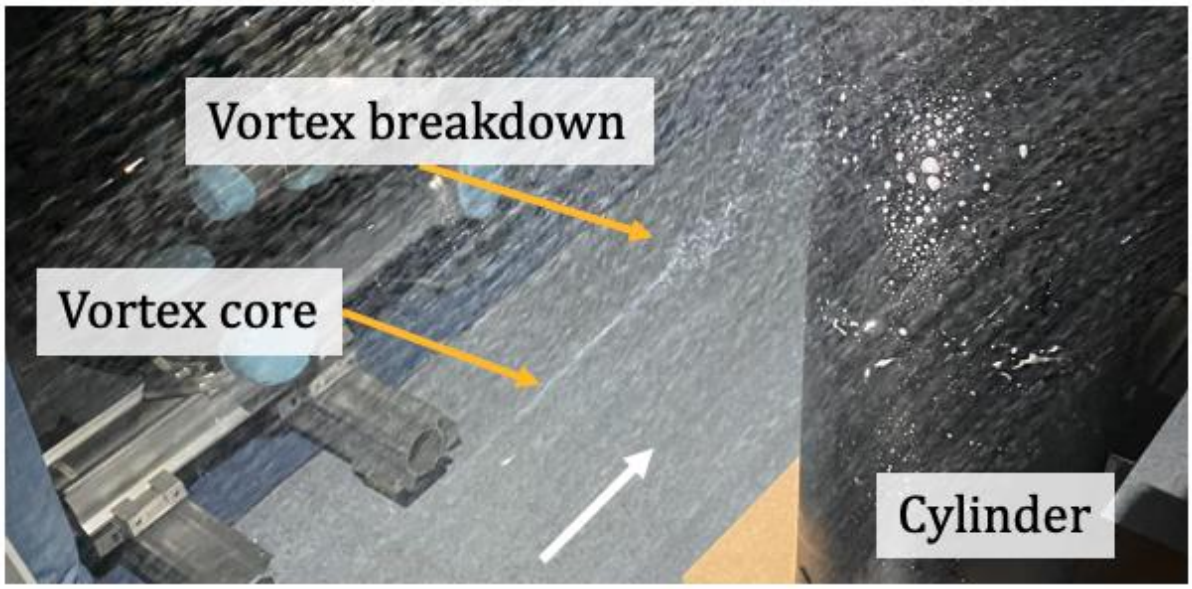

Figure 4.5*: Vortex core visualization with HTA HFSB. The freestream direction is indicated with the white arrow, and the vortex and its breakdown with yellow arrows.*

After establishing a ratio of helium and soap, the angle of attack was determined to be $\alpha = 5^\circ \pm 1$. Figure **4.6** and Figure **4.7** show the results of an e^n-method calculation at this angle of attack using XFOIL for $U_\infty = 8$ m/s and 12 m/s, which give a chord Reynolds number of approximately $6.3 \cdot 10^4$ and $9.5 \cdot 10^4$, respectively.

The dashed line represents the inviscid pressure coefficient ($C_p = (p - p_\infty)/q_\infty$) and the yellow and blue lines represent the viscous pressure coefficient. Yellow indicates the upper surface (suction side) and blue the lower surface (pressure side). On the *x*-axis, the chordwise location is indicated. In the lower graph, the boundary layer is illustrated. In both Figure **4.6** and Figure **4.7** can a laminar separation bubble and its reattachment be recognized by the bump in the yellow line of the C_p graph. It can be concluded that the flow does not separate fully at both Reynolds numbers. It was qualitatively tested that a vortex was generated at each of the freestream velocities at this angle of attack. Furthermore, due to the point of rotation near the trailing edge of the airfoil, the vortex is naturally aligned with the center of the cylinder.

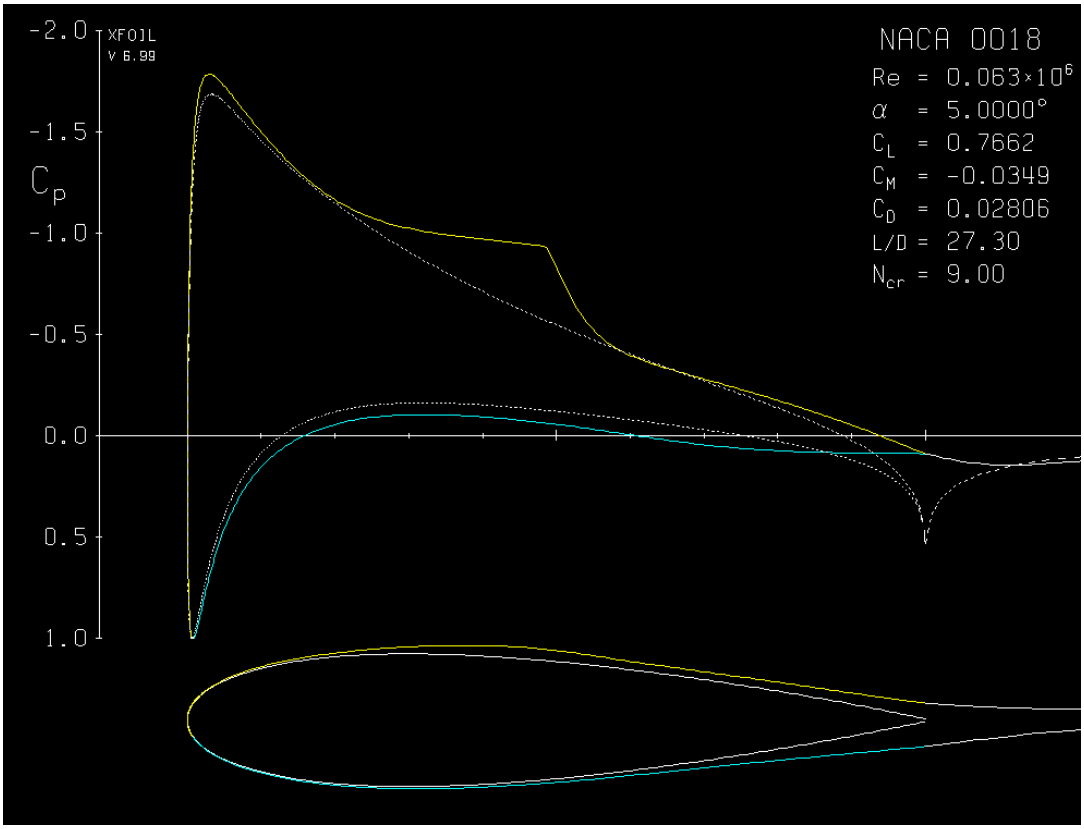

Figure 4.6: *Results of XFOIL for $U_\infty = 8$ m/s.*

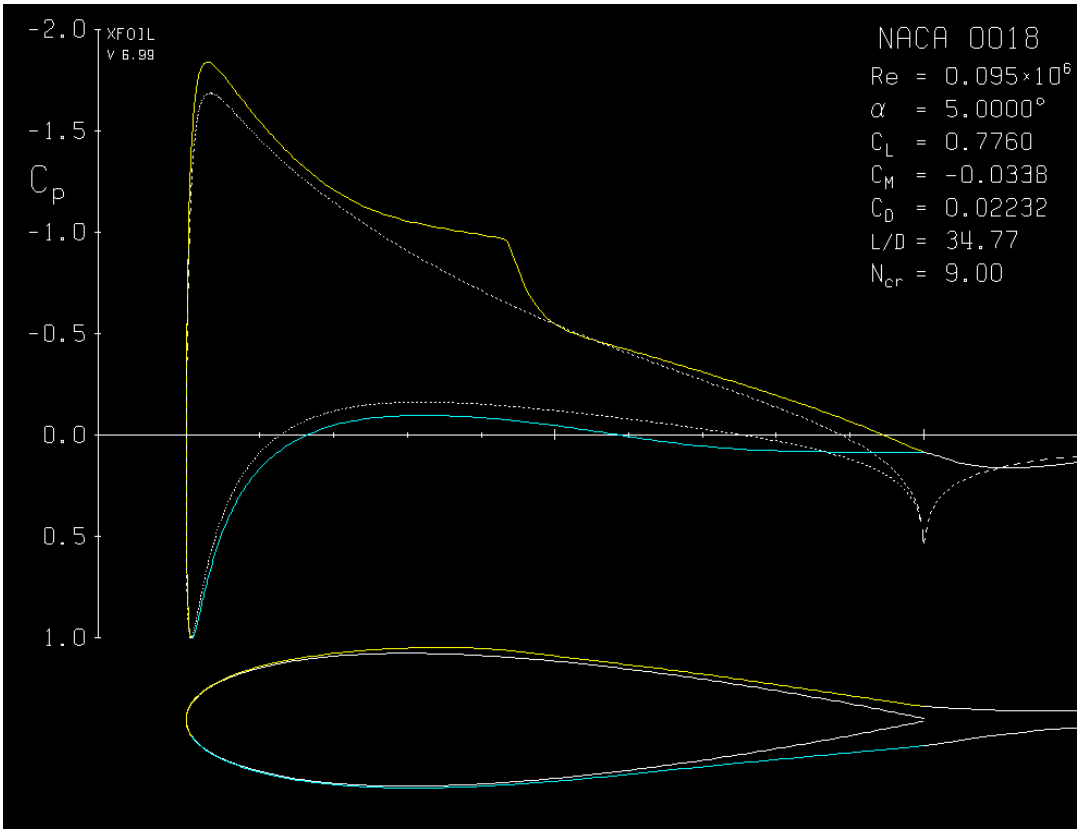

Figure 4.7: *Results of XFOIL for* $U_\infty = 12$ *m/s.*

The robotic CVV system was used for this experimental cammpaign. It consisted of the *LaVision MiniShaker Aero* and a *Universal Robots UR5* collaborative robotic arm. The MiniShaker houses four CMOS imagers in a diamond arrangement and an optical fiber in its center. The active camera sensors count 640 x 476 pixels and acquire images at 600 Hz through 4 mm lenses. The optical fibre transmits the light generated by the *Quantronix Darwin-Duo Nd-YLF* laser, which provided pulse energy (25 mJ per pulse at 1 kHz). The robot allows for motion in six degrees of freedom, similar to a human arm with a shoulder, elbow, and wrist. The CVV is mounted at the robot hand and the base is placed just outside the flow field. The base is considered to be the origin of the coordinate system by the robot. However, this was translated to the trailing edge of the airfoil for convenience. The robot is programmed using *RoboDK* to translate along the streamwise vortex toward its breakdown at the cylinder without interfering with the flow field.

To ensure overlap such that the entire x_{cyl} can be captured, multiple imaging locations are required, see Figure **4.8**. For the tests with $x_{cyl} = 50$ cm, it takes 1000 images at three different locations to capture the particle tracks in the entire measurement volume, for $x_{cyl} = 75$ cm it stopped to record at five locations, and for $x_{cyl} = 100$ cm at six locations. Using *LaVision Davis 10* these measurement volumes were processed using Shake-the-Box, merged and binned. To converge the estimate of the average velocity within a bin, its size was chosen such that a sufficient number of uncorrelated velocity measurements are captured

(Schneiders, Scarano, Jux, & Sciacchitano, 2018). The bins had, therefore, a subvolume size of 36 voxels with 75% overlap. The height of the measurement volume is approximately 20 cm which corresponds to 476 pixels. This means that the bin size is around 1.5 cm x 1.5 cm x 1.5 cm. A second-order polynomial regression is used to get the velocity inside a bin.

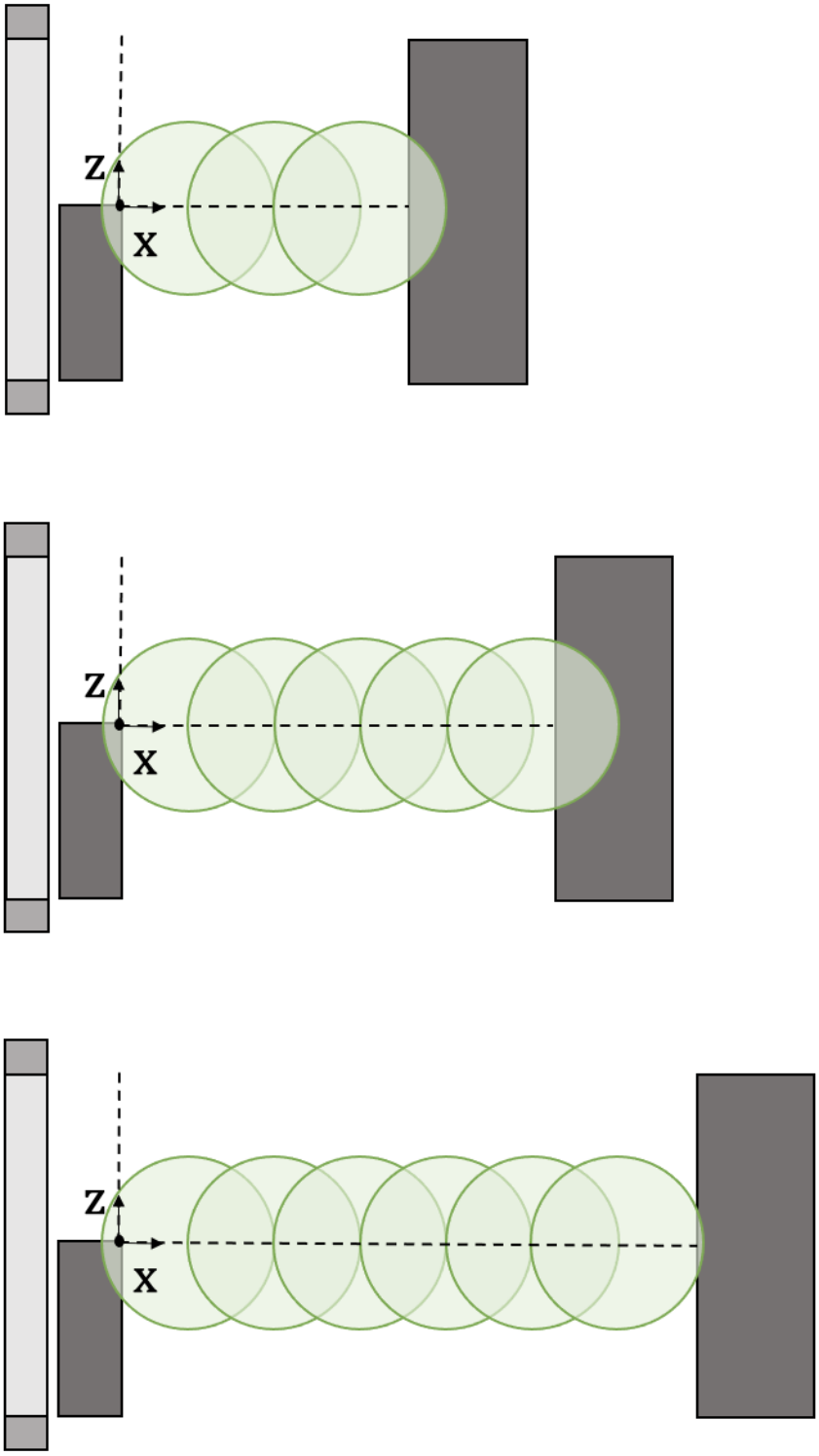

Figure 4.8: *Schematic of the imaging locations relative to the cylinder and the wing.*

Note that before any recording can be done successfully, the position of the robot and the cameras must be calibrated. The geometric calibration plate was integrated with the splitter plate. When calibrating, this plate is moved into the field of view of the robot. Furthermore, a volume self-calibration was completed which removes any residual calibration disparities using recorded particle images.

4.2 Vortex Detection

To detect a free, streamwise vortex from the acquired data, the behavior of the vortex core radius, tangential velocity, and streamwise vorticity were analyzed along the *x*-direction. The vortex core was located by searching for a circular velocity deficit or surplus in a plot of the *u*-component of the velocity, which represents a wake-like or jet-like vortex respectively. Additionally, the concentration of streamwise vorticity was analyzed to indicate the location of the core of the vortex more robustly.

To comply with the uncertainty of the particle position estimation, the streamwise vorticity and tangential velocity were extracted for a value of constant *z*, as the values in the depth direction (*y*-axis) of the CVV might be inaccurate (Schneiders, Scarano, Jux, & Sciacchitano, 2018). Figure **4.9** shows a schematic representation of these values. $U_{\theta,max}$ was calculated using the peak values of the *w*-component of the velocity, see Equation (4.1). Using the location of these peak values, the vortex core size was determined, see Equation (4.2).

$$U_{\theta,max} = \frac{w_{max} - w_{min}}{2} \qquad (4.1)$$

$$r_c = \frac{|y_{max} - y_{min}|}{2} \qquad (4.2)$$

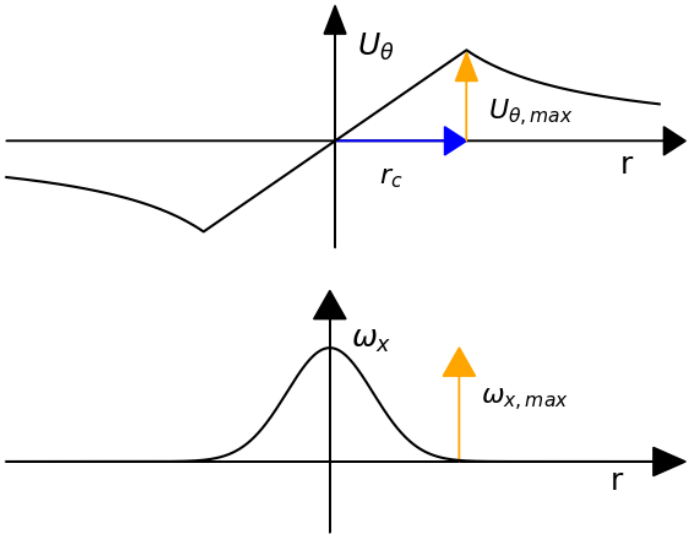

***Figure 4.9**: Schematic representation of the values of U_θ (calculated using the Rankine vortex model) and ω_x in the vortex core.*

The streamwise vorticity, ω_x, was extracted from the processed data from *Davis 10.* Here, the streamwise vorticity was determined along Equation (4.3). The absolute value of the peak at the vortex core will be taken as the vortex rotated clockwise as seen from the positive x-direction and has therefore negative streamwise vorticity. In the possible, but undesirable, scenario of insufficient development of a vorticity peak in the core of the vortex, i.e., the vorticity is in a ring-like structure, the average of the double-peak will be taken to calculate $|\omega_{x,max}|$.

$$\omega_x = \frac{\partial w}{\partial y} - \frac{\partial v}{\partial z} \qquad (4.3)$$

All of the above was implemented in a purpose-written Python 3.9 program.

4.3 Identification of Vortex Breakdown

The three-dimensional velocity field of each run case was discretized by the bin size of the *Davis* data processing. Therefore will the breakdown location be approximated by analyzing the values of $U_{\theta,max}$, r_c, and $|\omega_{x,max}|$ for different positions in x. The three-dimensional dataset is thus analyzed in two dimensions.

These properties of the vortex were initially analyzed at a 2 cm interval in x. From these results, the step size was iteratively refined around the rapid increase in vortex core radius, drop in tangential velocity, and drop in streamwise vorticity. The location of this sudden change in behavior is identified as the preliminary breakdown location on which the line fit is based. For the line in the pre-breakdown regime, the points from the airfoil until the estimated breakdown + 5 cm is taken, and for the post-breakdown line, the points from the estimated breakdown – 5 cm until the cylinder were taken. The lines were fitted based on each analyzed parameter ($U_{\theta,max}$, r_c, and $|\omega_{x,max}|$) after which the average of the determined breakdown locations is taken as the actual breakdown location of that run.

4.4 Definition of Local Flow Properties

Potential Flow Theory

One of the research objectives is to establish the relation between the location of the breakdown and the local flow properties, such as the adverse pressure gradient induced by the cylinder. Therefore, the local pressure gradient must be known. As the vortex interacts with the pressure field in the experimental data, it is chosen to use potential flow theory to extract the local adverse pressure gradient.

Potential flow theory is based on the assumption that the flow is inviscid, incompressible, and irrotational. Thus, the curl of the velocity field, the vorticity, is

zero. Therefore, it is possible to introduce the velocity potential, ϕ, see Equation (4.4). This must satisfy the Laplace's equation as shown in Equation (4.5).

$$U = \nabla\phi \tag{4.4}$$

$$\nabla^2\phi = 0 \tag{4.5}$$

The system is solved using cylindrical coordinates (Equation (4.6)), which describe the Laplace equation as Equation (4.7). Here is r the distance away from the cylinder center and θ the angle.

$$x = r\,cos(\theta), \quad y = r\,sin(\theta) \tag{4.6}$$

$$\frac{1}{r}\frac{\partial}{\partial r}\left(r\frac{\partial\phi}{\partial r}\right) + \frac{1}{r^2}\frac{\partial^2\phi}{\partial\theta^2} = 0 \tag{4.7}$$

Far away from the cylinder, the flow is considered uniform and at the boundary (r=R) it is stagnant, see Equation (4.8) and Equation (4.9) for these boundary conditions, respectively.

$$U_\infty = u\,i + 0\,j \tag{4.8}$$

$$U_R \cdot \hat{n} = 0 \tag{4.9}$$

The solution that satisfies these boundary conditions is Equation (4.10) and the velocity components in polar coordinates follow, see Equation (4.11) and Equation (4.12) (Acheson, 1990).

$$\phi(r,\theta) = u\,r\left(1 + \frac{R^2}{r^2}\right)cos(\theta) \tag{4.10}$$

$$U_r = \frac{\partial\phi}{\partial r} = u\left(1 - \frac{R^2}{r^2}\right)cos(\theta) \tag{4.11}$$

$$U_\theta = \frac{1}{r}\frac{\partial\phi}{\partial\theta} = -u\left(1 + \frac{R^2}{r^2}\right)sin\,(\theta) \tag{4.12}$$

As the flow is considered inviscid and irrotational, Bernoulli's equation can be used to calculate the pressure at a certain location from the cylinder, see Equation (4.13). Here is $U = \sqrt{U_r^2 + U_\theta^2}$.

$$p = \frac{1}{2}\rho(u^2 - U^2) + p_\infty \qquad (4.13)$$

A comparison based on experimental data and potential flow theory was performed to confirm the pressure field induced by the cylinder in the experiment was similar to potential flow theory. Here, the deceleration of the flow field is measured and compared.

Normalized Pressure Gradient

To determine the relation between the vortex breakdown location and the local pressure gradient, a definition for a critical, normalized pressure gradient was proposed. This new definition was based on the expression for a local pressure gradient in the *x*-direction, see Equation (4.14) and hereafter referred to as ∇p. The value of p will be determined based on potential flow theory described above.

$$\nabla p_x = \lim_{\Delta x \to 0} \frac{\Delta p}{\Delta x} \qquad (4.14)$$

For normalization of the definition in Equation (4.14) it is chosen to use the dynamic pressure of the freestream ($q_\infty = \frac{1}{2}\rho U_\infty^2$) and the vortex core radius, see Equation (4.15).

$$\nabla p^* = \lim_{\Delta x \to 0} \frac{\Delta p}{\Delta x} \Big/ \frac{q_\infty}{r_c} \qquad (4.15)$$

The critical, normalized pressure gradient is the value for ∇p^* determined at the breakdown location, see Equation (4.16).

$$\nabla p^*_{bd} = \lim_{\Delta x \to 0} \left(\frac{\Delta p}{\Delta x}\right)_{bd} \Big/ \frac{q_\infty}{r_{c,bd}} \qquad (4.16)$$

The breakdown location will be generalized by correcting it with the distance at which the cylinder is located, see Equation (4.17). To ensure that the results are intuitive, the *x*-axis is inverted such that upstream is to the left and downstream is on the righthand-side on the graph.

$$\Delta x_{bd} = x_{cyl} - x_{bd} \qquad (4.17)$$

Reynolds Number

The results will also be presented in terms of the Reynolds number. The Reynolds number depicts the ratio between the inertial and viscous forces. Equation (4.18) is based on the freestream velocity and is similar to the Reynolds number in the

experiments of Sarpkaya (Sarpkaya, Effect of the Adverse Pressure Gradient on Vortex Breakdown, 1974).

$$Re_{U_\infty} = \frac{2r_{c,bd}U_\infty}{\nu} \qquad (4.18)$$

Sarpkaya also introduces the normalized circulation to showcase the experimental results. However, as the angle of attack was kept constant, the circulation was constant in this experiment. Literature suggests that the angle of attack and the tip shape have a strong influence on the tip vortex behavior (Lee & Pereira, 2010). As these were constant throughout the experiment, it was expected that the vortex would be relatively similar per run (i.e., the same value for the ratio for metrics such as U_θ/U_∞).

5. Results & Discussion

The results of the experimental campaign are discussed and divided in subcategories. First will the flow topology be discussed. Then, the detection and structure of the vortex will be elaborated upon. Following, the identification of vortex breakdown and the estimation of its location is discussed. Last, the relation to local flow parameters is presented.

5.1 Flow Topology

To get a better understanding of the influence of the vortex and the cylinder separately, results are presented of tests where either object was inserted in the flow. In Figure **5.1**, Figure **5.2**, and Figure **5.3** the absolute streamwise vorticity is visualized for different locations in *z.* The airfoil is indicated in black and its trailing edge is the origin of the coordinate system. The airfoil is plotted at $\alpha = 0°$, but during the experiment it was rotated at $\alpha = 5° \pm 1°$ to produce the vortex. The bin size is indicated as the black square in the lower right corner. It was found that the vortex wandered towards the positive *z*-direction, i.e., upwards. Therefore, the *xy*-plane is presented at z = 0 cm, 1 cm, and 2 cm. This is also illustrated by the schematic in the top right corner. From the plots in Figure **5.1**, Figure **5.2**, and Figure **5.3**, it can be observed that the vortex does not break down as no sudden change in its structure was observed. Furthermore, the vortex seemed to wander towards the negative *y*-direction, which is the direction of the wake of the airfoil and towards the robot.

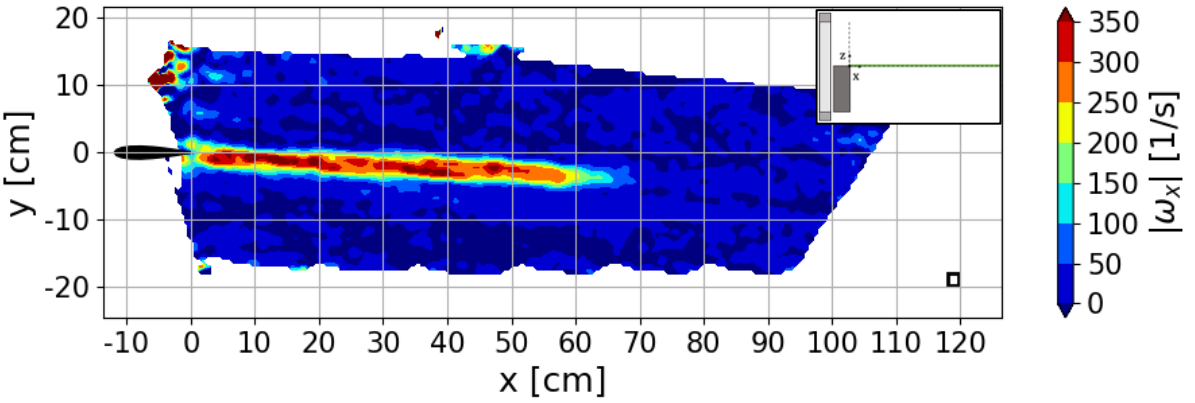

Figure 5.1: *Streamwise vorticity contour plot for vortex only. At U_∞ = 10 m/s and z = 0 cm.*

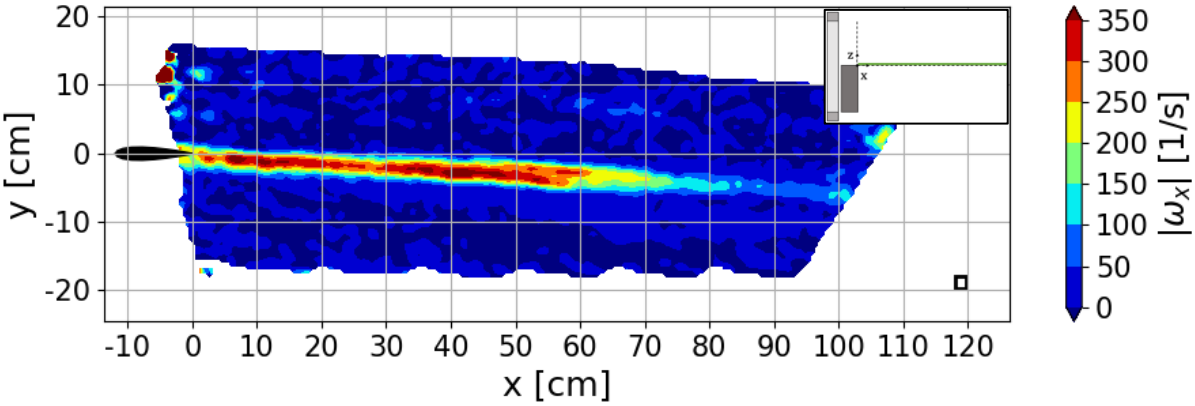

Figure 5.2: *Streamwise vorticity contour plot for vortex only. At U_∞ = 10 m/s and z = 1 cm.*

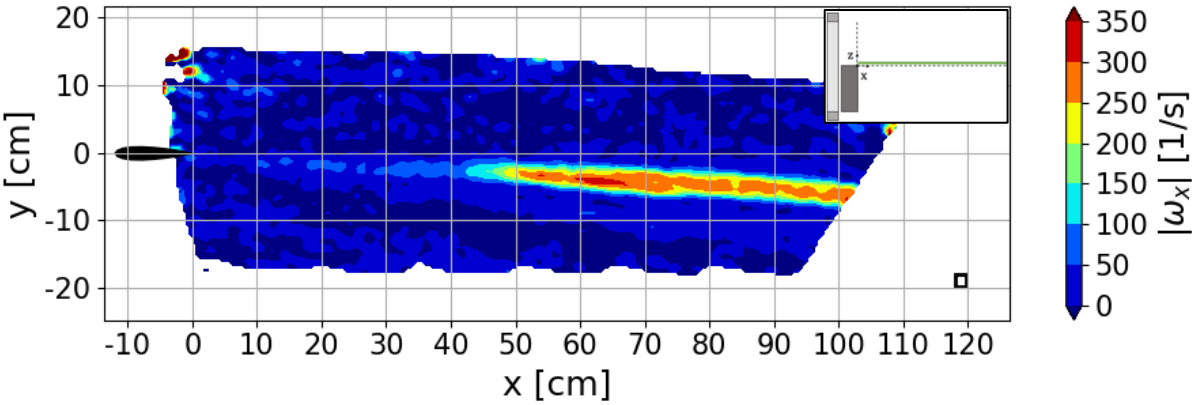

Figure 5.3*: Streamwise vorticity contour plot for vortex only. At U_∞ = 10 m/s and z = 2 cm.*

Figure **5.4** shows the ratio between the u-component of the velocity and the freestream velocity where only the cylinder was introduced to the flow field. The contour lines of this same ratio, calculated using potential flow theory, are visualized with dark grey lines. The plot shows that the velocity decreases towards the cylinder. This means that the flow field is obstructed by the cylinder. The robot's field of view is also obstructed by the cylinder and the laser reflection of the cylinder has interfered with the data acquisition. The reflection effects are recognized as the signal drop close to the cylinder and the sudden increase in velocity at approximately x = 45 cm, which is unlikely.

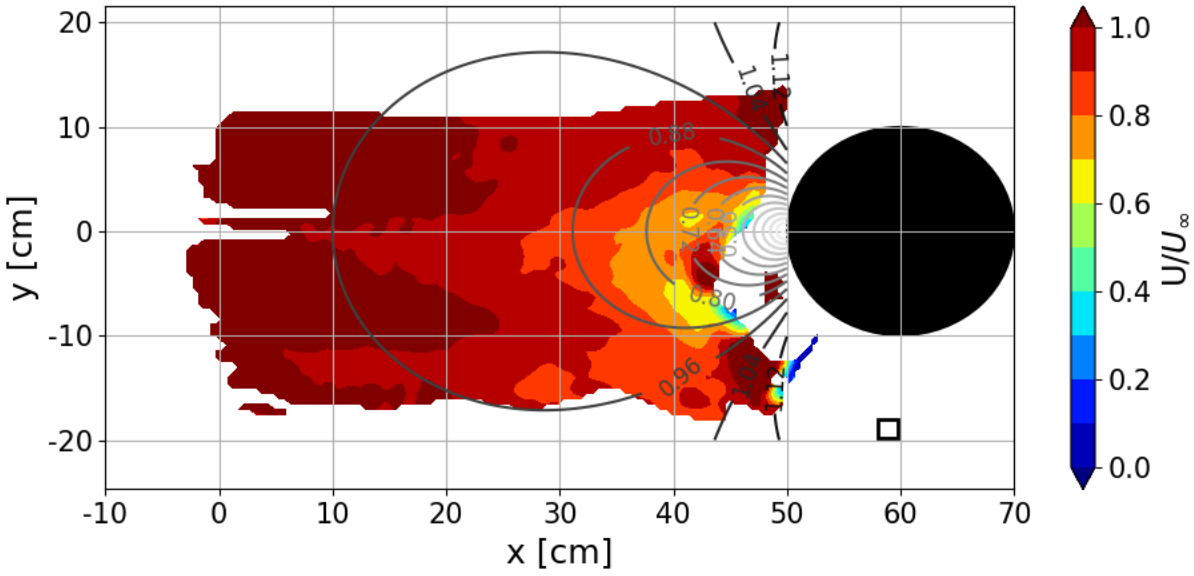

***Figure 5.4**: Filled contour plot for the u-component of the velocity divided by the freestream velocity at U_∞ = 10 m/s for the cylinder only. The dark contour lines show the results of this ratio for potential flow theory.*

Figure **5.5** illustrates the comparison between the experimental data of Figure **5.4** in blue where no vortex was present and the potential flow theory in orange. The values for u, v, and w are extracted at $y = 0$ cm and the velocity magnitude is calculated. This comparison shows that the general trend of the decrease in velocity in front of the cylinder is similar to the calculated case. There is a lack of data close to the cylinder, but as the data already shows a decrease of over 50%, it is assumed that the cylinders' pressure field behaves similarly to potential flow theory. Therefore, the values of potential flow theory are used in the determination of the pressure gradient at the breakdown location.

The blue line shows signs of some noise in the data field. This noise could have been reduced by taking more images and averaging the data over a bigger sample size. The increase in velocity around x = 45 cm is probably a side-effect of the hereabove mentioned reflection.

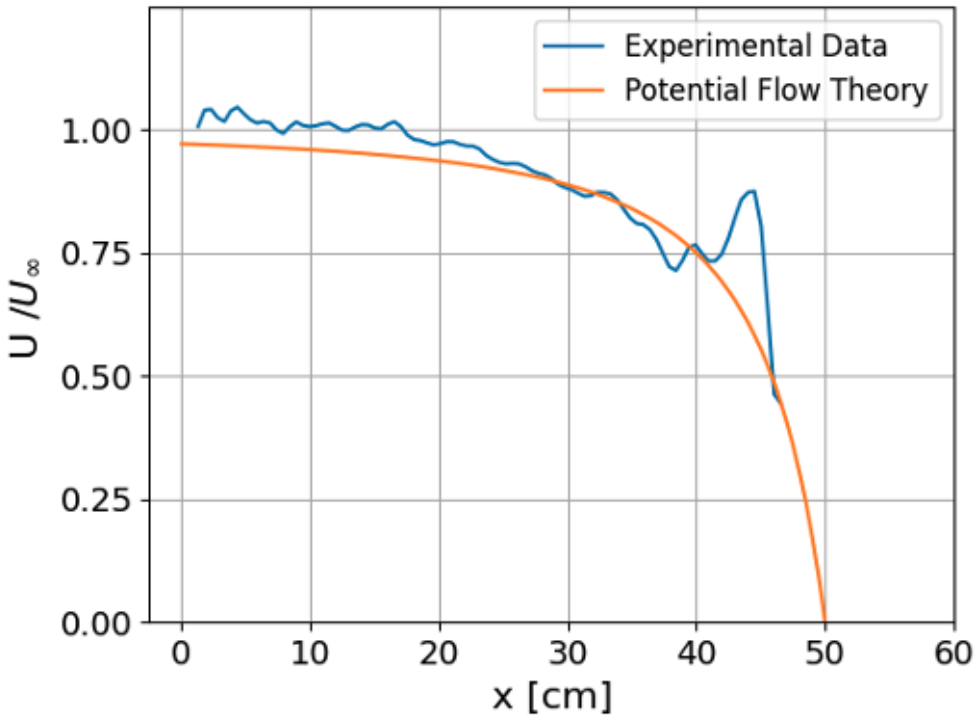

Figure 5.5: *Comparison of experimental data and potential flow theory for* $x_{cyl} = 50$ *cm.*

Control of Experiment

From the results thus far, it seems that the coordinate system of the data has rotated slightly. It was observed during the experiment that the vortex traveled straight onto the cylinder. However, from Figure **5.1**, Figure **5.2**, and Figure **5.3** it seems that the vortex wanders toward the negative *y*-direction. Furthermore, the signal drop in the data of Figure **5.4** indicates that the upstream edge of the cylinder might have been around y = -5 cm and x = 45 cm instead of y = 0 cm and x = 50 cm as it would have blocked the acquisition of data in that position.

During the experimental campaign, the set-up was secured such that components could not move during the experiments. The cylinder could only travel along x when unscrewed. It appears that the set-up might have shifted by, for example, vibrations caused by the flow. The determination of the relative position of the trailing edge of the airfoil and the robot base (the original origin of the system) was done only once at the beginning of the experiment. Furthermore, the airfoil was vastly secured at its angle of attack, but it was only checked if the airfoil was rigid throughout the experiments, not the possible shift in the angle of attack.

As a final remark, the experimental campaign took place in a two-week period in November 2022. There was construction done on the building and students and staff were able to access the W-Tunnel room anytime. There was no control of the set-up after its initial build, which might have led to inaccurate readings of spatial coordinates. However, as most data processing is dependent on the structure of

the vortex itself and the determination of the breakdown location will have a systematic error, it is chosen to not correct this shift.

5.2 Vortex Detection and Structure

Vortex Detection

The data of Figure **5.6** is extracted at the $x = 20$ cm plane for $U_\infty = 12$ m/s and $x_{cyl} = 75$ cm. The vectors are added to indicate the v- and w-components of the velocity. The black square in the bottom right corner shows the bin size for reference. The graph only shows the velocity where data was found, i.e., gaps exist where no data was recorded.

By looking at the filled contour plot of the u-component of the velocity in Figure **5.6**, the vortex can be detected as the circular velocity surplus around y = -2 cm and z = 0 cm. This indicates that the produced wing tip vortex is jet-like (Délery, 1994). The jet- or wake-like nature of a vortex is dependent on the airfoil angle of attack and the tip vortex interaction with the wing wake (Lee & Pereira, 2010). Literature suggests that the cross-over from wake- to jet-like is around $\alpha = 7°$ for a NACA0012. As the experiments were conducted at a constant angle of attack of $5° \pm 1°$ and the wing consistently produced a jet-like vortex, a specific number of this cross-over cannot be given for a NACA0018 airfoil. However, literature suggests that wake-like vortices are produced at smaller angle of attacks, so the cross-over must be at $\alpha < 5° \pm 1°$ (Lee & Pereira, 2010).

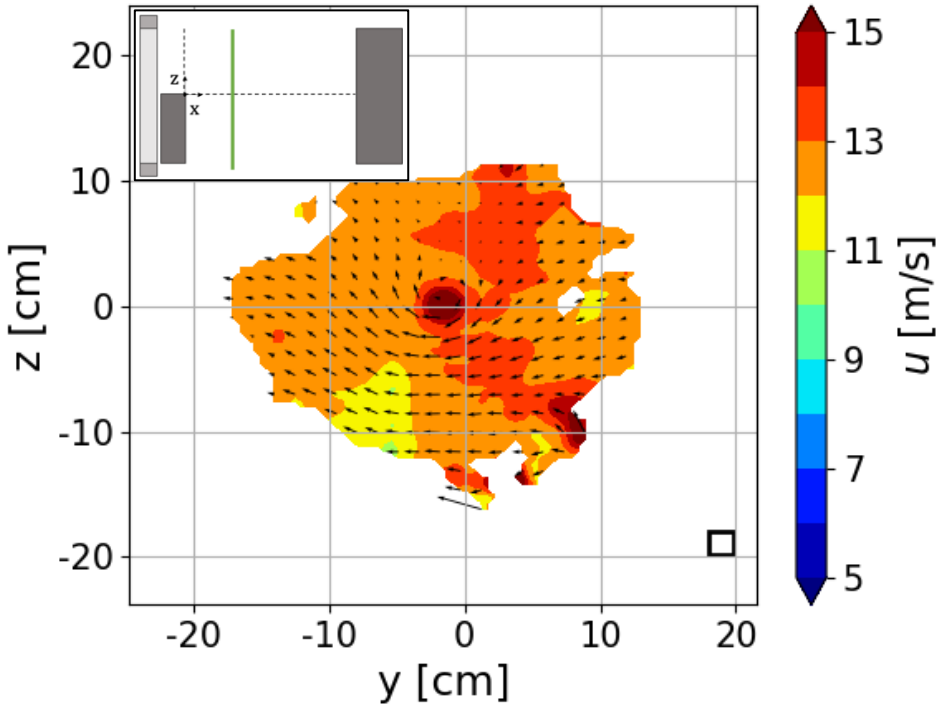

Figure 5.6: U-component of the velocity at x = 20 cm for U_∞ = 12 m/s and x_{cyl} = 75 cm.

In combination with the direction of the vectors, the location of the vortex can be identified. However, to determine the position of the vortex more accurately by eye, a plot of the streamwise vorticity is suggested, such as Figure **5.7**. Note, that the determination of the vortex core location is done manually, thus it could include user bias. Furthermore, the determination of the location is conducted on millimeter scale which entails that the location includes a ±0.5 mm error. However, the data is processed on centimeter scale, thus this error is insignificant. Furthermore, the data in Figure **5.6** shows a fluctuation of ±1 m/s in the freestream velocity. Both plots, and the ones previously discussed, show some edge effects. This is an artifact of the system.

In Figure **5.7** it is observed that the streamwise vorticity is concentrated around the same location of the velocity surplus in Figure **5.6**, such that it is the location of the vortex. However, the vorticity is not concentrated as a maximum at the center of the vortex core. This indicates insufficient development of the roll-up of the vortex sheet into the free vortex. This could be the result of the geometry of the half-span wing. Research has shown that flat wing tips (such as the one in this experiment) produce multiple secondary vortices which create a messier tip vortex, as opposed to a rounded tip which creates a cleaner and more concentrated vortex (Lee & Pereira, 2010).

Furthermore, the data in both Figure **5.6** and Figure **5.7** do not show any gaps (i.e., signal drop) in the location of the vortex core. This implies that the seeding of the HFSB was sufficient throughout the vortex. As observed during the experiment, the HFSB did concentrate around the center of the vortex. Even though the seeding was sufficient, it was not homogeneous.

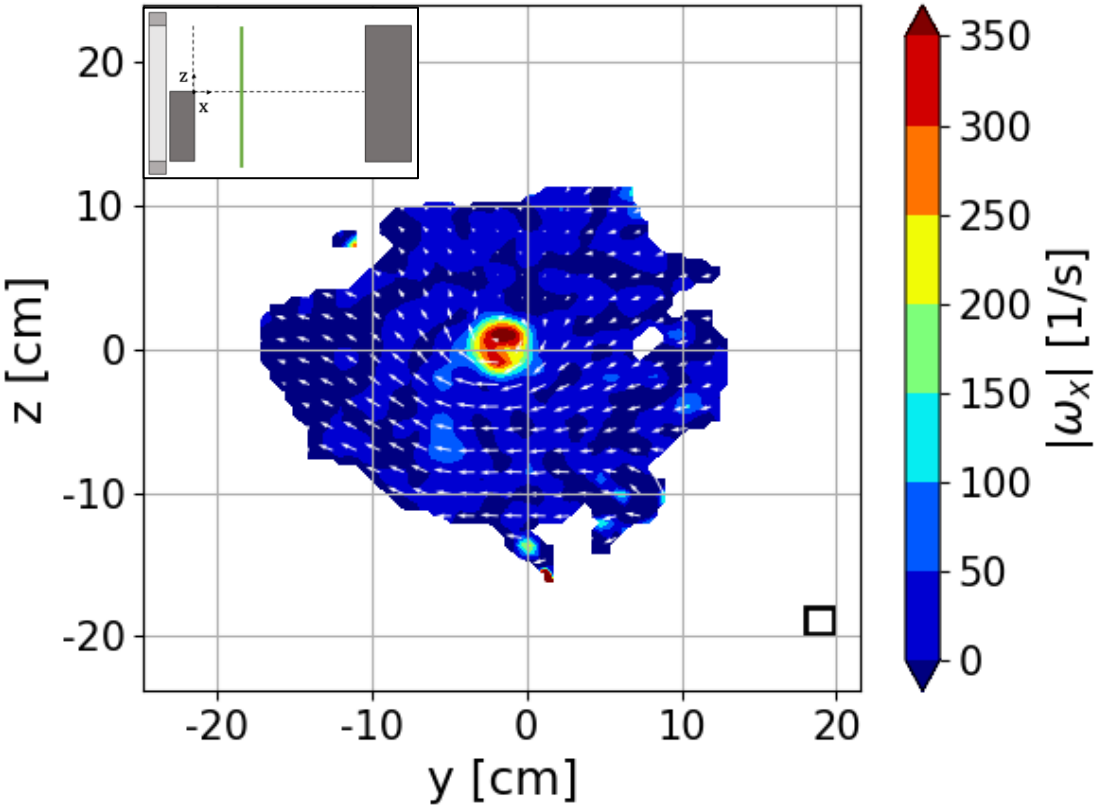

Figure 5.7: *Absolute streamwise vorticity at $x = 20$ cm for $U_\infty = 12$ m/s and $x_{cyl} = 75$ cm.*

Vortex Structure

The internal vortex structure is evaluated along a line of constant z at the vortex core. The z-direction is chosen as the estimation of the particle position of the CVV in the depth (y) direction could be inaccurate (Schanz, Gesemann, & Schröder, 2016). The data in Figure **5.8** shows the u-component of the velocity normalized with the freestream velocity for x_{cyl} = 75 cm at x = 20 cm across the vortex core. Here, as well as the contour plot in Figure **5.6**, can the velocity surplus at the vortex core be observed. Furthermore, the axial flow at a higher freestream velocity is relatively low as opposed to a low freestream velocity. However, multiple studies suggest that the Reynolds number has little to no effect on the variation of the core axial velocity, but the angle of attack does (McAlister & Takahashi, 1991; Lee & Pereira, 2010). As it was intended to keep the angle of attack of the experiment constant, it can be concluded that the wing might have shifted in between measurements and caused this difference.

Some flow abnormalities are present as well. First, the lines outside the vortex core for 10 m/s and 12 m/s are around $U_{axial}/U_\infty = 1$, whereas $U_\infty = 8$ m/s is slightly higher. This is a consequence of the error margin observed in the freestream velocity in Figure **5.6**, which is 12.5% for $U_\infty = 8$ m/s. Second, the lines fluctuate in the region further away from the robot (i.e., the positive y direction). The geometric calibration was done with the calibration plate at the y = 0 cm plane, so these fluctuations could be an artifact of the system's capability to reconstruct outside its calibrated field of view.

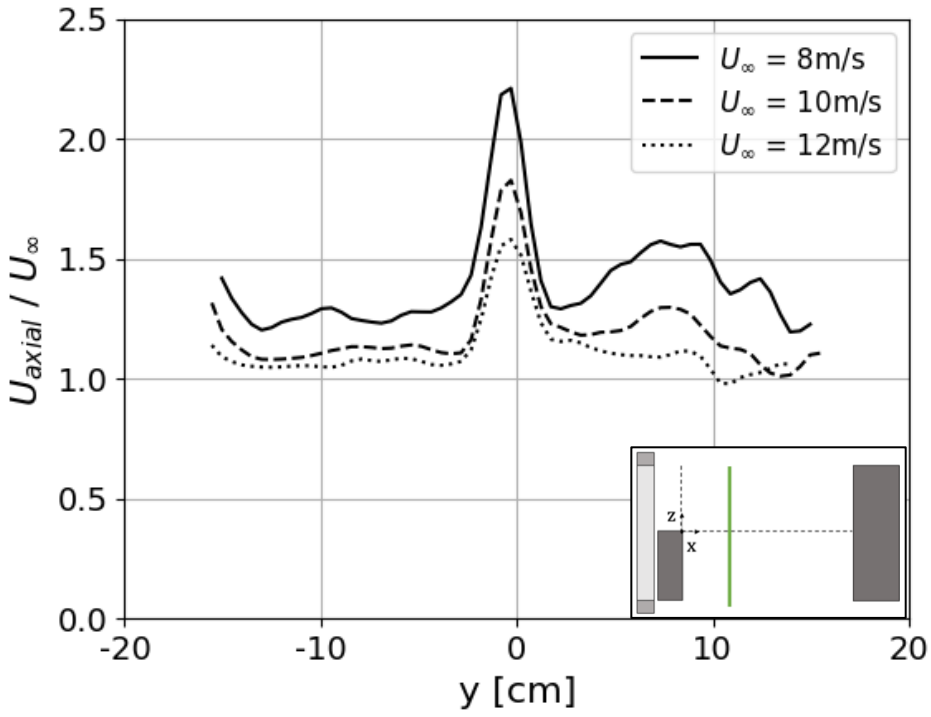

Figure 5.8: *U-component of the velocity normalized by U_∞, for x_{cyl} = 75 cm at x = 20 cm across the vortex core.*

Figure **5.9** shows the distribution of the tangential velocity normalized with the freestream velocity over the vortex core for x_{cyl} = 75 cm at x = 20 cm. The vortex core radius is defined as the distance from the center to the peak of tangential velocity as indicated in the figure. Equation (4.1) and Equation (4.2) are used to calculate the vortex core radius and the maximum tangential velocity.

From the comparison between the values of the tangential velocity over the different freestream velocities, it is found that their peaks are relatively close, but differ nevertheless. The average difference from the mean peak value is approximately 9%. As the circulation of each of these vortices is constant, the core radius must change between these vortices as well. However, the difference between the core radii for these different values of the freestream velocity is zero. This is a consequence of the discretization of the dataset. The spatial resolution is *too low* to analyze the internal vortex structure. To illustrate, for a vortex in the pre-breakdown regime such as Figure **5.9**, the core radius is approximately 2 cm, which means that the core diameter is only 7 bins wide. Hence, the error margin of ±0.5 bin per radius is unsatisfactory. Furthermore, similarly to the data in Figure **5.8**, fluctuations in the data are present in the area further away from the robot.

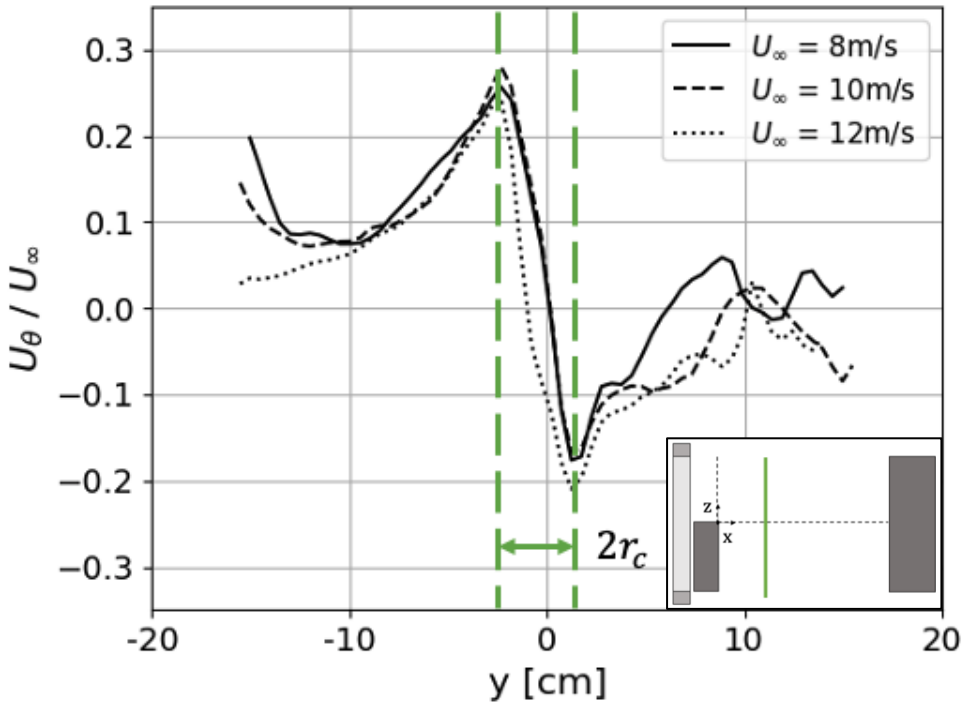

Figure 5.9: *Tangential velocity normalized by U_∞, for x_{cyl} = 75 cm at x = 20 cm across the vortex core.*

Figure **5.10** illustrates the distribution of streamwise vorticity over the vortex core. As a consequence of the insufficient development of the vorticity in the vortex core, the streamwise vorticity has a double peak, instead of a single peak. The streamwise vorticity is also negative, as the pitch angle of the airfoil ensured a counterclockwise rotating airfoil as seen from the wind tunnel. Therefore, as observed from the positive *x*-direction, the vortex rotates clockwise thus the vorticity is negative. The value for $|\omega_{x,max}|$ is determined by taking the absolute average of these double peaks. Similar to the velocity profiles in Figure **5.8** and Figure **5.9**, fluctuations in the data are noticeable in the area further away from the robot.

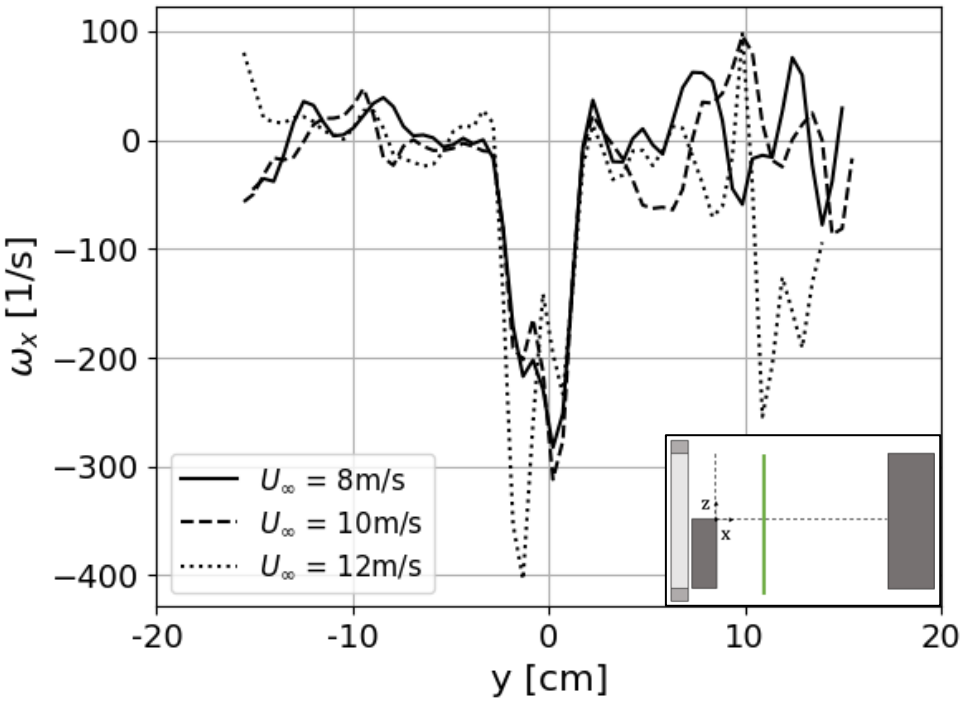

Figure 5.10: *Streamwise vorticity for x_{cyl} = 75 cm at x = 20 cm across the vortex core.*

5.3 Vortex Breakdown Identification and Location

Vortex Breakdown Identification

Figure **5.11** illustrates the absolute streamwise vorticity for U_∞ = 12 m/s and x_{cyl} = 75 cm at z = 1.5 cm. From this graph, a drop in vorticity can be observed around x = 50 cm, as well as a slight increase in the region of concentrated vorticity, i.e., the vortex core. These developments of the vortex core indicate that the vortex has broken down. These developments were not present in the vorticity field of the vortex only (Figure **5.1**, Figure **5.2**, and Figure **5.3**) and it can therefore be concluded that the pressure field induced by the cylinder is causing the vortex to break down.

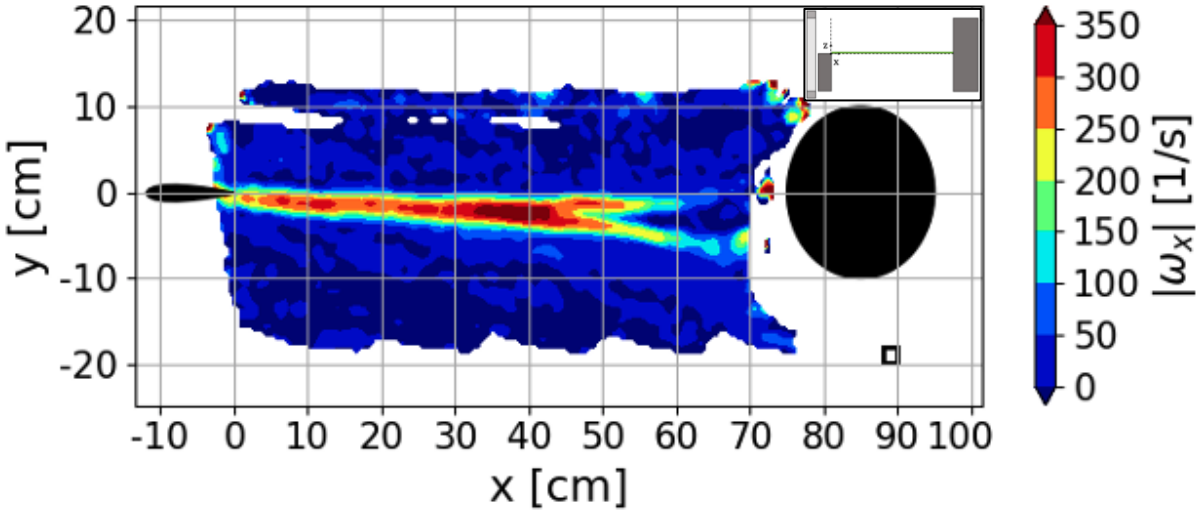

***Figure 5.11**: Absolute streamwise vorticity at z = 1.5 cm for U_∞ = 12 m/s and x_{cyl} = 75 cm.*

Preliminary Estimation of the Vortex Breakdown Location

A preliminary estimation of the breakdown location based on the development of the vortex core in the x-direction is shown in Figure **5.12**. The results for U_∞ = 8 m/s are shown in red, U_∞ = 10 m/s in green, and U_∞ = 12 m/s in blue. The dashed black lines show the location of the cylinder. The colored dashed lines indicate the estimations of the breakdown location for x_{cyl} = 50 cm (top graph), x_{cyl} = 75 cm (middle graph), and x_{cyl} = 100 cm (bottom graph).

The black solid line shows that the vortex development over x = 100 cm where no cylinder was present is minimal. This is in agreement with what is found in literature. Studies suggested that tip vortices show little growth or decay over the first 20 or more spans downstream of the wing (Chiffone, 1974; Iversen, 1976). The colored solid lines show the development of the vortex core radius of the vortices that encountered the cylinder. Here, the sudden deviation from the black line indicates the breakdown and this position has been marked as the estimation

for the line-fitting in the next step of processing the data and is indicated as colored dashed lines.

It should be noted that the analysis of the sudden deviation from the '*no cylinder*' data set is affected by the discretization of the data. This could have led to inaccurate estimations of the breakdown location, which affects the resulting breakdown location.

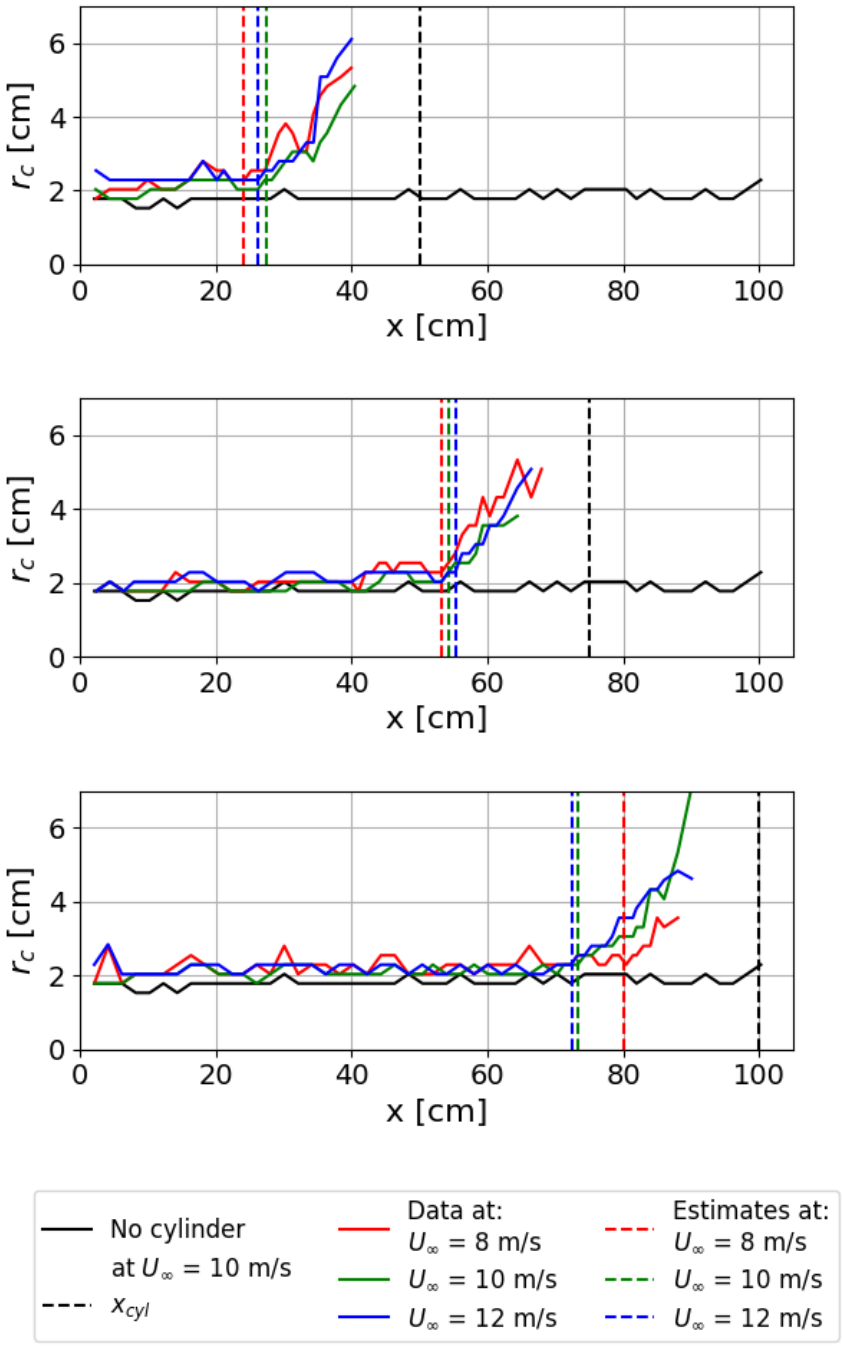

Figure 5.12: *Estimates of the vortex breakdown location using the development of the vortex core radius.*

Estimation of the Vortex Breakdown Location

Figure **5.13**, Figure **5.14**, and Figure **5.15** illustrate the process of estimating the breakdown location of the vortex based on the development in the vortex core radius, the streamwise vorticity, and the tangential velocity, respectively. The data of these graphs showcase the behavior of the vortex for U_∞ = 12 m/s and x_{cyl} = 75 cm.

The dashed lines each show a linear fit through the data points of the pre- and post-breakdown regimes. These regimes are based on the estimation of Figure **5.12** and extended 5 cm. The intersection of these lines determines the breakdown location. The final breakdown location of each run is the average of the determinations based on these three metrics. The resulting breakdown location measured from the cylinder, Δx_{bd}, can be found in Table 1 for each variation of the runs.

***Table 1**: Results of the Δx_{bd} estimation for each variation of parameters.*

U_∞ \ x_{cyl}	**50 cm**	**75 cm**	**100 cm**
8 m/s	24.465 cm	23.864 cm	26.049 cm
10 m/s	22.239 cm	21.954 cm	27.115 cm
12 m/s	23.941 cm	21.231 cm	28.027 cm

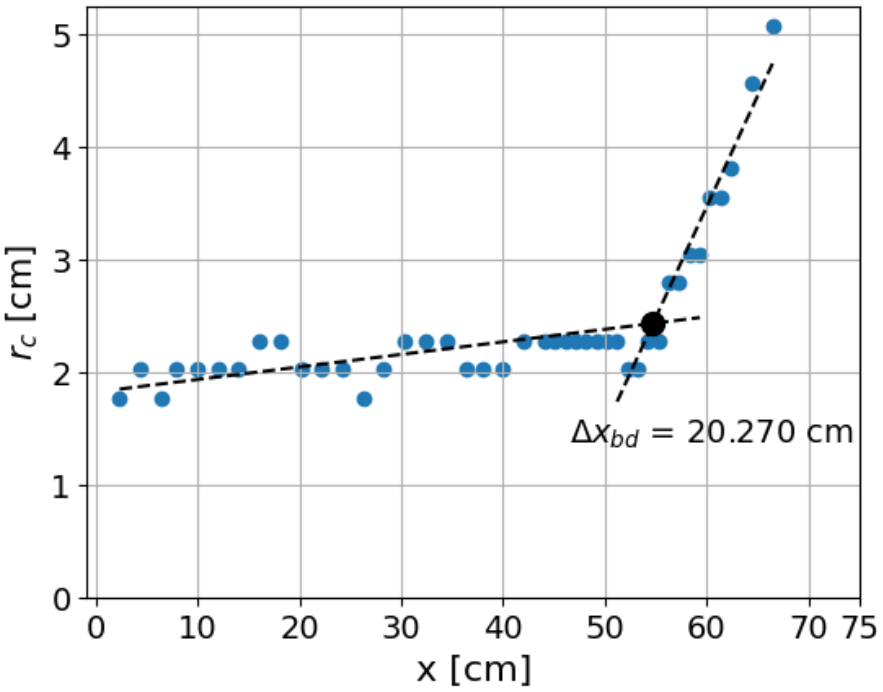

***Figure 5.13:** Line-fitting to determine the breakdown location through pre- and post-breakdown regimes of the development of the vortex core radius for U_∞ = 12 m/s and x_{cyl} = 75 cm.*

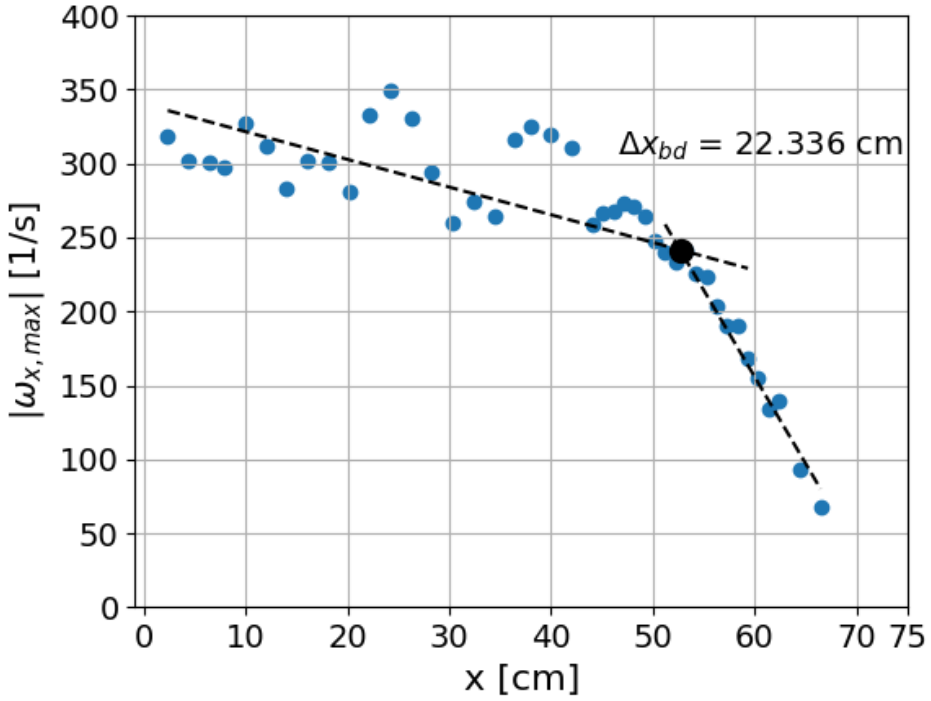

Figure 5.14: *Line-fitting to determine the breakdown location through pre- and post-breakdown regimes of the development of the maximum, absolute streamwise vorticity for* $U_\infty = 12$ *m/s and* $x_{cyl} = 75$ *cm.*

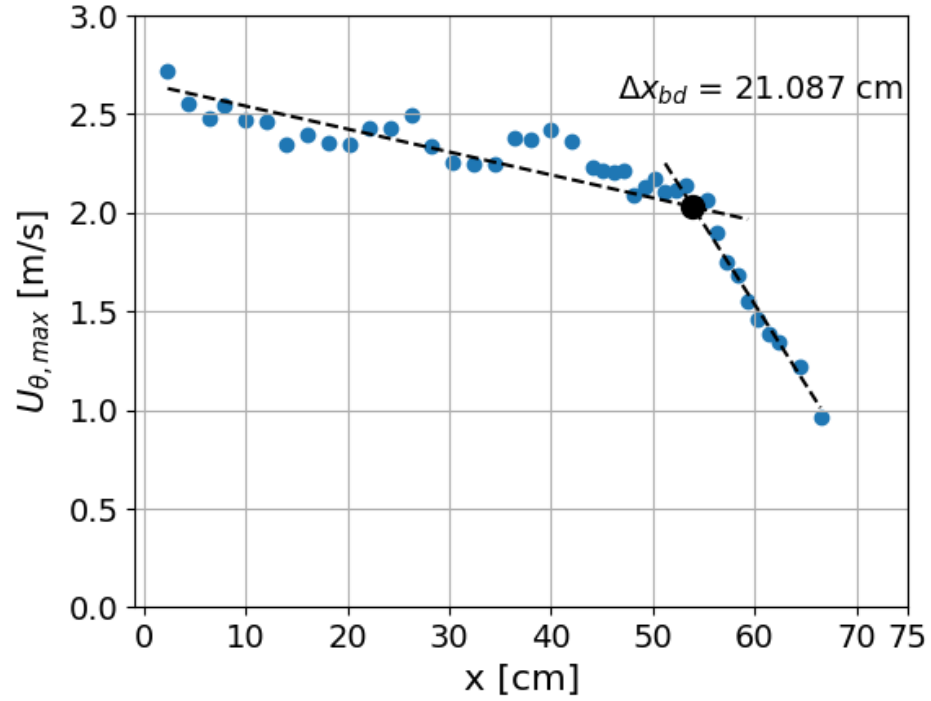

Figure 5.15: *Line-fitting to determine the breakdown location through pre- and post-breakdown regimes of the development of maximum tangential velocity for* $U_\infty = 12$ *m/s and* $x_{cyl} = 75$ *cm.*

5.4 Relation to Local Flow Parameters

Relation between Vortex Characteristics and Local Flow Parameters

Figure **5.16** illustrates the relationship between the maximum tangential velocity at the breakdown location and the freestream velocity. The legend shows that the results are categorized by color for the different values of the freestream velocities (red for 8 m/s, green for 10 m/s, and blue for 12 m/s) and by marker for different values of the cylinder distance (triangles for 50 cm, squares for 75 cm, and circles for 100 cm). The figures hereafter use the same color scheme and type of markers to indicate the difference between the runs, hence the legend is only included in this figure.

As the circulation was kept constant throughout the experiment, the ratio between the maximum tangential velocity and the freestream velocity is assumed to be constant (Lee & Pereira, 2010). By fitting a linear line through the points, it is evident that there is a large spread of the data points. The outliers are located at approximately ±40% of the ratio $U_{\theta,max,bd}/U_{\infty}$. As this is a significant error margin, the following results which are affected by this parameter are greatly influenced by this inaccuracy.

Following the conservation of angular momentum and the resulting increase in tangential velocity, the general trend of the vortex core radius must decrease. Figure **5.17** visualizes the relation between the vortex core radius at the breakdown location and the freestream velocity. A hand-drawn linearization has been plotted with the grey, dashed line and shows this decaying trend. Similar to the tangential velocity, the vortex core radii at the breakdown location are mostly outliers.

These outliers are undesirable, but certain to happen based on how the data was obtained. The velocity of Figure **5.16** is acquired using inhomogeneous seeding throughout the vortex core. Additionally, the location of the data in Figure **5.17** is obtained from a low spatial resolution data set

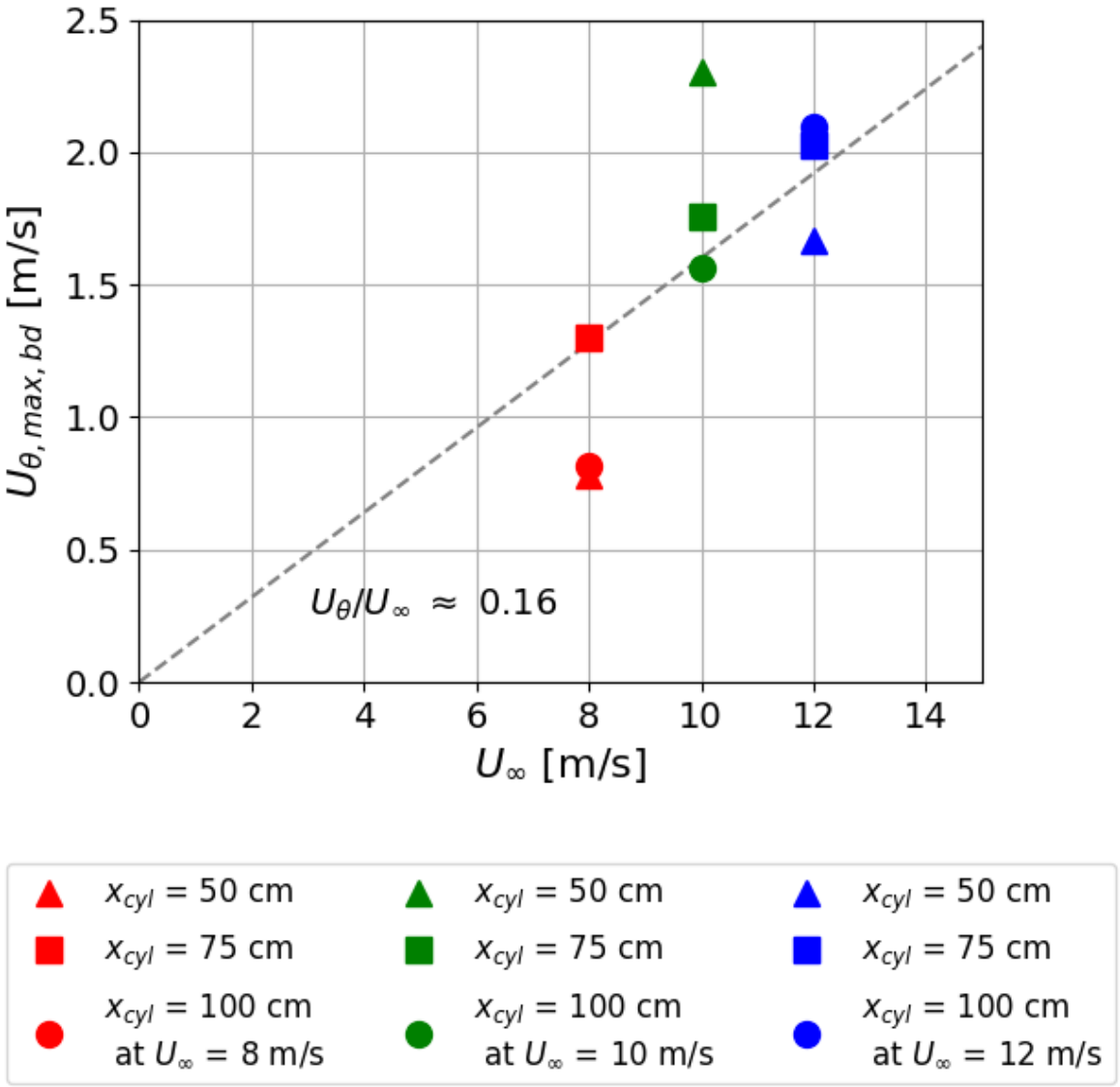

Figure 5.16: *Maximum tangential velocity at the breakdown location for different freestream velocities. The grey, dashed line is an estimated linearization of the relation between these parameters.*

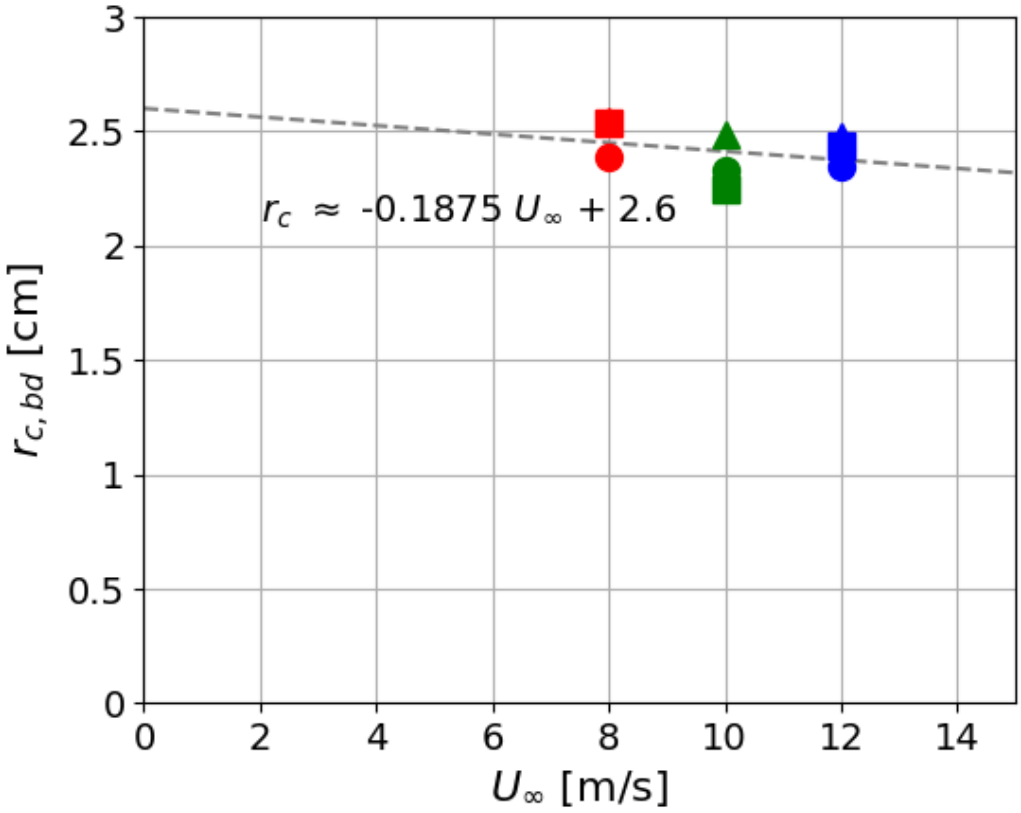

Figure 5.17: *Vortex core radius at the breakdown location for different freestream velocities. The grey, dashed line is an estimated linearization of the relation between these parameters.*

Relation between the Breakdown Location and Local Flow Parameters

A definition for the normalized pressure gradient at the breakdown location was proposed in Equation (4.16) as well as the definition for the breakdown location as measured from the cylinder in Equation (4.17). The intent of the definition in Equation (4.16) was to identify which value of the pressure gradient was critical, i.e., which value of the pressure gradient would induce vortex breakdown. If the pressure gradient was the sole driver of vortex breakdown, each point should be at the same value for ∇p^*_{bd}.

The results presented in Figure **5.18** show a linear trend. The breakdown occurs upstream for a higher value of this critical, normalized pressure gradient. However, this is a causality of the nature of the pressure gradient. As the pressure field is induced by a cylinder, the pressure increases downstream. Thus, when the breakdown occurs more downstream, the pressure is inherently higher. Therefore, the results of Figure **5.18** must not be confused with the results of the experiments of Sarpkaya (Figure **2.8**) where a higher *constant* pressure gradient induced vortex breakdown more upstream (Sarpkaya, Effect of the Adverse Pressure Gradient on Vortex Breakdown, 1974).

As previously concluded, the pressure field of the cylinder is the dominant driver of vortex breakdown. However, the breakdown location does not correlate with a constant value of the normalized pressure gradient. Consequently, it must be dependent on other local flow parameters.

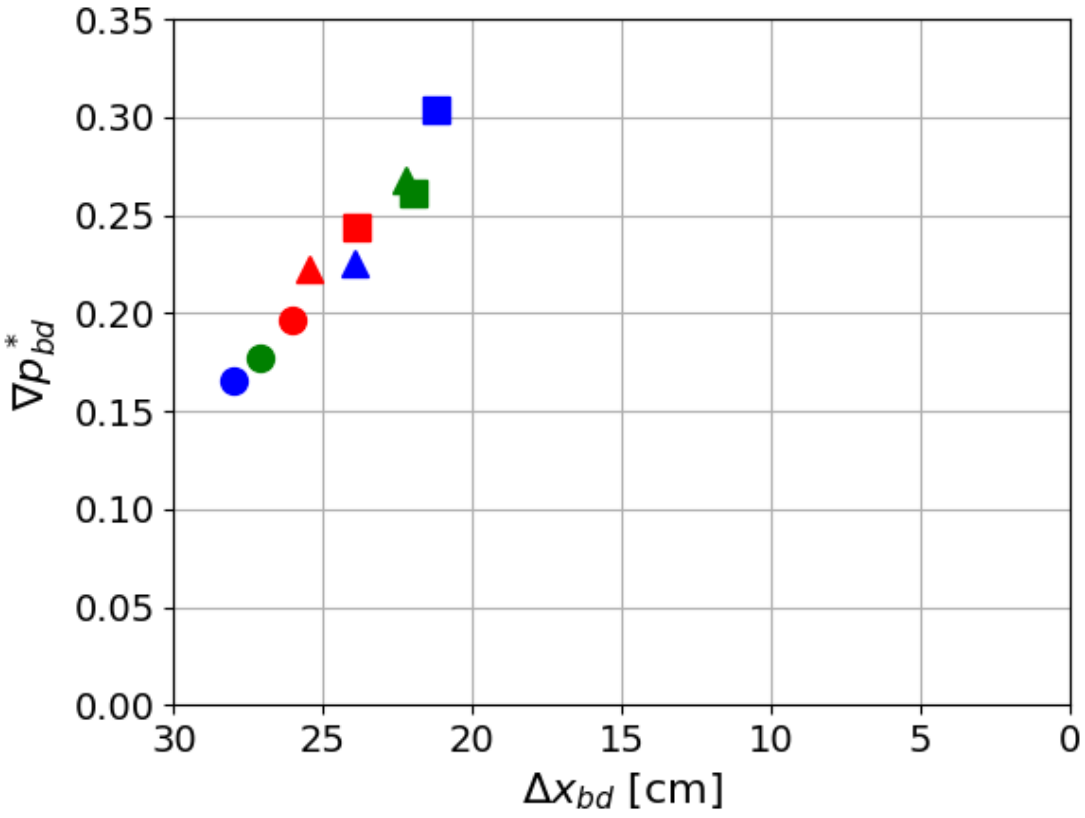

Figure 5.18: *Relation between the normalized pressure gradient at the breakdown location and the breakdown location as measured from the cylinder.*

The relation between the Reynolds number based on the freestream velocity and the breakdown location is shown in Figure **5.19**. This Reynolds number is dependent on the vortex core radius (Equation (4.18)) and the freestream velocity. From the results in Figure **5.6** the freestream velocity includes an error margin of ±1 m/s. Additionally, the results of Figure **5.17** show that the determination of the vortex core radii are mostly outliers from its general trend. Consequently, these values of the Reynolds number are affected by these errors and are prone to be incorrect.

Literature suggests that a relation should exist between the Reynolds number and the location of vortex breakdown (Sarpkaya, Effect of the Adverse Pressure Gradient on Vortex Breakdown, 1974). However, from the lack of correlation in Figure **5.19**, it can be concluded that the effect of the Reynolds number is barely measurable with the robotic volumetric PIV system and did not offer conclusive results.

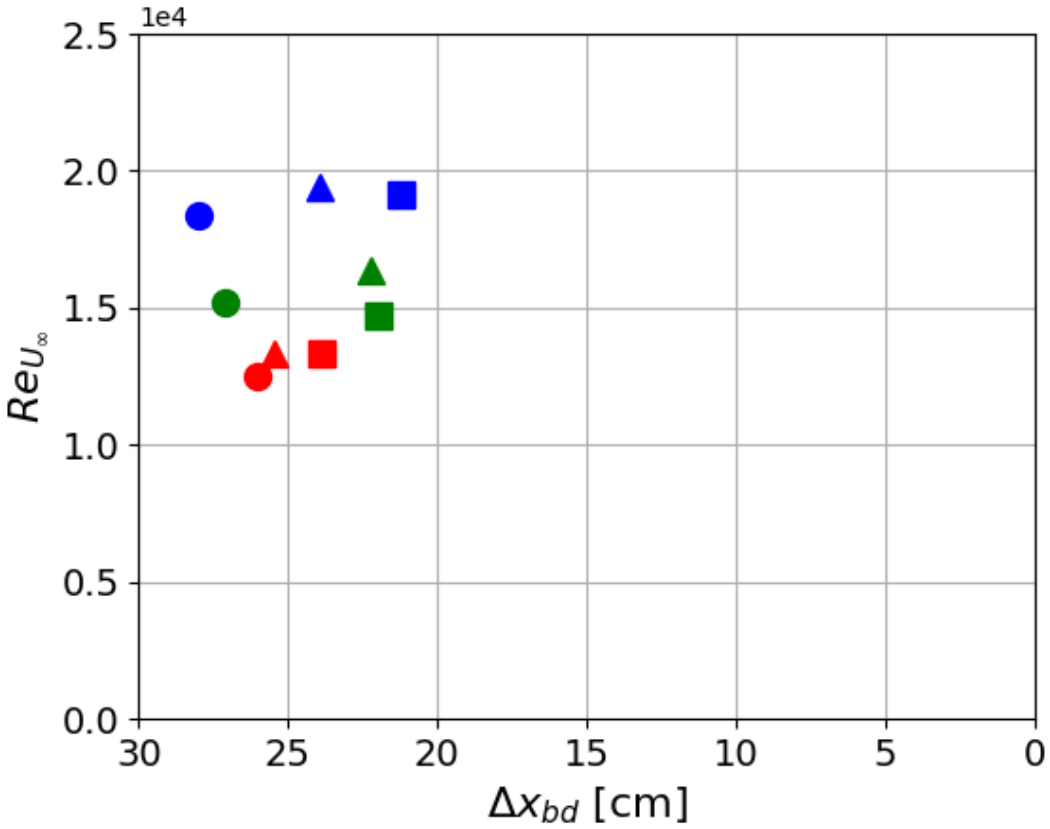

Figure 5.19: *Relation between the Reynolds number based on the freestream velocity and the breakdown location as measured from the cylinder.*

6. Conclusions & Recommendations

6.1 Conclusions

The objective of this thesis was to assess the feasibility of measuring a free, streamwise vortex and its breakdown from data acquired with robotic volumetric PIV, whilst analyzing the relation between the local flow properties and the location of the breakdown. The results of this exploratory and experimental study illustrated the capabilities and limitations of the robotic volumetric PIV to analyze vortex dynamics.

The use of HFSB ensured no signal drop in the vortex, but still concentrated around the vortex center. From the streamwise vorticity data, the wing tip vortex structure associated with a flat tip was recognized. Furthermore, the anomalous development of the vortex when interacting with the induced pressure field was identified as well. This breakdown of the vortex only occurred when the vortex encountered the cylinder-induced pressure field.

Given the inaccuracy (i.e., low spatial resolution) of the robotic system, the structure of the vortex pre- and post-breakdown could be recognized. However, further analysis of the vortex's internal structure or its relation to local flow properties was greatly affected by this inaccuracy. Due to these effects, the results concerning the relation between the local flow properties and the location of the breakdown were inconclusive. The system is, in these configurations, not capable of measuring a free, streamwise vortex and its breakdown.

6.2 Recommendations

While working on this thesis, a number of limitations were identified, and additional tests were deemed necessary. Unfortunately, due to time constraints, it was not possible to address these issues or conduct further experiments. Consequently, the following recommendations are proposed based on experimental insights and areas for future research.

Experimental Considerations

A general recommendation to ensure more accurate results during similar experimental campaigns is to actively control the experiment. The circulation is of

great influence on the tip vortex's behavior and can be controlled by changing the angle of attack of the wing. Even though the wing was tightly secured at an angle of attack, it should have been checked that the airfoil was still fixed at a constant angle of attack for each measurement. Also, the freestream velocity appeared to include some fluctuations throughout the flow field. It was observed that these fluctuations were ±1 m/s. By taking more images per measurement the effect of these fluctuations on the data could have been minimized.

Furthermore, the half-span wing had a flat tip which introduced secondary vortices to the tip vortex. This was recognized by the ring-like formation of the streamwise vorticity. To exclude this behavior, a rounded wing tip would be recommended. Additionally, the accuracy of the vortex characteristics (the streamwise vorticity, the tangential velocity, and the core radius) could have been increased by obtaining data points over different azimuthal positions instead of a line at constant *z.*

The location of the vortex core was manually identified by analyzing the location of the concentration in streamwise vorticity and the circular velocity surplus. This might have included a user bias. The error that this bias included was ±0.05 cm (approximately 2.5% of the pre-breakdown vortex core radius) and therefore regarded as insignificant. The experimental set-up aimed to produce an isolated vortex, so a more in-depth analysis was unnecessary. For more complex flow fields an analysis based on the Q-, λ_2-, or Γ_2- criterion to identify the vortex is recommended.

Finally, each variation of the flow properties was only measured once. Both repetitions of measurements and repetition of data analysis is recommended. The first can either confirm odd behavior or mark it as an outlier, the latter can mitigate user bias.

Future Work

Several improvements are recommended for future experimental research on the influence of local flow properties on vortex breakdown. First, an increase in spatial resolution is recommended when the robotic system is used. However, one would need a higher particle density to decrease the bin size, which would be challenging as vortices are inhomogeneously seeded due to their pressure distribution. Therefore, the application of an interpolation method would suffice as well. This will lead to a more accurate reconstruction of the vortex structure, thus more accurate results of the vortex characteristics at the breakdown location. However, using a system with a larger tomographic aperture in combination with LPT would also aid in achieving more accurate data. However, this system is more complex in its set-up, which makes tracking the development of the vortex over a long distance laborious.

Second, literature suggests that circulation is of great influence. Hence, ensure control of the circulation of the experiment by precisely changing and securing the angle of attack of the half-span wing. Third, if the effects of the vortex development on the occurrence of breakdown are investigated, allow for the vortex to develop for a relatively long distance. Literature states that the vortex will change behavior at a minimum of 20 wing spans downstream. Therefore, change the span of the wing or increase the size of the set-up. Finally, a larger range in freestream velocity, thus Reynolds number, is advised. With a larger range, the Reynolds number effects should become more noticeable. This will provide insights into its effect on the breakdown location.

References

Acheson, D. (1990). Elementary Fluid Dynamics. Oxford: Clarendon Press.

Bhagwat, M. J., & Leishman, J. G. (2002). Generalized Viscous Vortex Model for Application to Free-Vortex Wake and Aeroacoustic Calculations. *58th Annual Forum and Technology Display of the Americal Helicopter Society International*.

Bosbach, J., Kühn, M., & Wagner, K. (2009). Large Scale Particle Image Velocimetry with Helium Filled Soap Bubbles. *Experiments in Fluids*, 539-547.

Caridi, G. C., Sciacchitano, A., & Scarano, F. (2017). Helium-Filled Soap Bubbles for Vortex Core Velocimetry. *Experiments in Fluids*, 1-12.

Chiffone, D. (1974). Correlation for Estimating Vortex Rotational Velocity Downstream Dependence. *Journal of Aircraft*, 716-717.

Délery, J. M. (1994). Aspects of Vortex Breakdown. *Progress in Aerospace Sciences*, 1-59.

Elsinga, G. E., Scarano, F., Wieneke, B., & van Oudheusden, B. W. (2006). Tomographic Particle Image Velocimetry. *Experiments in Fluids*, 933-947.

Escusier, M. (1988). Vortex Breakdown: Observations and Explanations. *Progress in Aerospace Sciences*, 189-229.

Faleiros, D. E., Tuinstra, M., Sciacchitano, A., & Scarano, F. (2019). Generation and Control of Helium-Filled Soap Bubbles for PIV. *Experiments in Fluids*, 1-17.

Günther, T., & Theisel, H. (2018). The State of the Art in Vortex Extraction. *Computer Graphics Forum*, 149-173.

Graftieaux, L., Michard, M., & Grosjean, N. (2001). Combining PIV, POD and Vortex Identification Algorithms for the Study of Unsteady Turbulent Swirling Flows. *Measurement Science and Technology*, 1422.

Grant, I. (1997). Particle Image Velocimetry: a Review. *Proceedings of the Institution of Mechanical Engineers, Part C: Journal of Mechanical Engineering Science*, 55-76.

Heyes, A. L., & Smith, D. (2005). Modification of a Wing Tip Vortex by Vortex Generators. *Aerospace Science and Technology*, 469-475.

Iversen, J. (1976). Correlation of Turbulent Trailing Vortex Decay Data. *Journal of Aircraft*, 338-342.

Jeong, J., & Hussain, F. (1995). On the Identification of a Vortex. *Journal of Fluid Mechanics*, 69-94.

Jux, C., Scarano, F., & Sciacchitano, A. (2019). Aerodynamic Pressure Reconstruction on Generic Surfaces from Robotic PIV Measurements. *Proceedings of the 13th International Symposium on Particle Image Velocimetry*.

Jux, C., Sciacchitano, A., Schneiders, J. F., & Scarano, F. (2018). Robotic Volumetric PIV of a Full-Scale Cyclist. *Experiments in Fluids*, 1-15.

Lee, T., & Pereira, J. (2010). Nature of Wakelike and Jetlike Axial Tip Vortex Flows. *Journal of Aircraft*, 1946-1954.

Massey, S., & Kandil, O. (1998). Effect of Apex Flap Deflection on Vertical Tail Buffeting. *36th AIAA Aerospace Sciences Meeting and Exhibit*, 762.

McAlister, K., & Takahashi, R. (1991). NACA0015 Wing Pressure and Trailing Vortex Measurements. National Aeronautics and Space Administration, Office of Management, Scientific and Technical Information Program.

Mitchell, A. M., & Délery, J. (2001). Research into Vortex Breakdown Control. *Progress in Aerospace Sciences*, 385-418.

Nieuwstadt, F. T., Boersma, B. J., & Westerweel, J. (2016). Turbulence. Springer.

Obert, E. (2009). Aerodynamic Design of Transport Aircraft. IOS Press BV.

Peckham, D., & Atkinson, S. A. (1957). Preliminary Results of Low Speed Wind Tunnel Tests on a Gothic Wing of Aspect Ratio 1.0.

Raffel, M., Willert, C. E., Scarano, F., Kähler, C. J., Wereley, S. T., & Kompenhans, J. (2018). Particle Image Velocimetry. Springer.

Rossow, V. J. (1999). Lift-Generated Vortex Wakes of Subsonic Transport Aircraft. *Progress in Aerospace Sciences*, 507-660.

Sarpkaya, T. (1971). On Stationary and Travelling Vortex Breakdowns. *Journal of Fluid Mechanics*, 585.

Sarpkaya, T. (1971). Vortex Breakdown in Swirling Conical Flows. *AIAA Journal*, 1792.

Sarpkaya, T. (1974). Effect of the Adverse Pressure Gradient on Vortex Breakdown. *AIAA Journal*, 602-607.

Scarano, F. (2013). Tomographic PIV: Principles and Practice. *Measurement Science and Technology*.

Schanz, D., Gesemann, S., & Schröder, A. (2016). Shake-The-Box: Lagrangian Particle Tracking at High Particle Image Densities. *Experiments in Fluids*, 1-27.

Schneiders, J. F., Scarano, F., Jux, C., & Sciacchitano, A. (2018). Coaxial Volumetric Velocimetry. *Measurement Science and Technology*.

Wang, C. Y., Gao, Q., Wei, R., Li, T., & Wang, J. (2016). 3D Flow Visualization and Tomographic Particle Image Velocimetry for Vortex Breakdown over a Non-Slender Delta Wing. *Experiments in Fluids*, 1-13.

Wieneke, B. (2013). Iterative Reconstruction of Volumetric Particle Distribution. *Measurement Science and Technology*.